Complete tool for predicting the mutual coupling in non-uniform arrays of rectangular aperture radiators

Terahertz Sensing Group

Delft University of Technology

31 October 2017

Zhengzheng Wang

[4518721]

Complete tool for predicting the mutual coupling in non-uniform arrays of rectangular aperture radiators

This thesis work has been performed at the Terahertz Sensing Group, Department of Microelectronics, Faculty of Electrical Engineering, Computer Science and Mathematics (EEMCS) of the Delft University of Technology, Delft, The Netherlands. This work will be defended in public on 2017-10-31. This thesis work has been supervised by dr.ir. Ioan. E. Lager.

The graduation committee consists of prof.dr. A. (Andrea) Neto, dr.ir. I. E. (Ioan) Lager. (EEMCS, TU Delft) and prof.dr.ir. M.J. (Mark) Bentum (Faculty of Electrical Engineering, Eindhoven).

Acknowledgement

I herewith would like to thank everyone who helped me in finishing the tough master courses and accomplishing the difficult task that has been writing this thesis.

I must express my gratitude to all my teachers in Teraherz Sensing Group: dr. Andrea Neto, dr. Nuria Llombart and dr. Daniele Cavallo. I experienced a really difficult time studying electromagnetics in my first master year with a dilettante and frivolous attitude. Spending almost 6 months extra, they offered their great patience and kindness helping me finally open the door of the electromagnetics. During the time, I settled down myself and learnt how to learn things. I believe it is of great luck to meet those nice teachers in my life and the appreciation will be kept for my lifetime.

My highest respect is for Ioan. E. Lager, a cool old man, who supervised my master thesis. He always has a clear view about steps to solve a problem and keeps rigorous towards the analysis. Although I at least disturbed him twice in his office every day and brought endless questions and requests, he is still gentle and kind, answering and making some odd jokes. We have worked together for my thesis and two papers during the last 9 months, and he taught me how to do research step by step and how to write proper txt word by word. One of the paper has been accepted by Antenna and Wireless Propagation Letters (AWPL), which is the best achievement I've ever made in my life. Words cannot describe how grateful I am for his kind help.

I ought to acknowledge as well the contribution and kindly help from Cristian Coman and Massimiliano Simeoni, where the idea of my thesis is based on their past achievements.

I would like to thank all my "roommates" and "colleagues" in the Teraherz Sensing Group. Although talking with a "far-east person" is not that fun, people here still try helping me work out difficulties and impress me with their interesting cultures and thoughts. In this way, my oral English also has improved a lot.

To my Chinese friends, Xuyang, Mingliang and Yichao, thank you so much for the great time we spent together.

Finally, to my parents, thank you for offering me the opportunity doing master abroad in TU Delft and I really appreciate your support for my self-willed decision on education and career.

王铮铮
Zhengzheng Wang

Delft, October 2017

Table of Contents

1 Introduction

1.1 Non-uniform Array Antenna

Non-uniform array antennas receive increasing attention due to their range of performance enhancements. This antenna concept can be applied in several areas:

1. Solution of non-uniform samples in practical circumstance, for example in a space-random acquisition process [1]-[3];

2. Sparse array design due to the merit of unfixed spacing, such as suppression of grating lobes in compact array [4], [5] and FMCW radar [6], or reduction of array elements [7];

3. Shared aperture antenna design, for instance filtering antenna array [8] and polarization-agile antenna [9].

However, a price is paid for these extra benefits. It is well known that the convenience of analysing finite uniform array antenna comes from the Floquet method with the assumption of infinite uniform array antenna, while non-uniform array structures cannot be solved by this efficient method due to its aperiodic structure. In practice, the simulation of non-uniform array antenna is a great burden on both time and machine resources. Strategies like deterministic thinning methods [10], [11], stochastic methods [12]-[15] and pseudo-random methods [16]-[18] have been studied to optimize the placement of array elements, while some techniques discussed in [6], [19]-[21] are developed to solve problems in feed performance and shared elements. But even so, most of the relative strategies elements are ideal and isotropic, for which there is always some significant difference between the simulation and measurement, especially when the array spacing is small in terms of wavelength. The phenomenon is caused mainly by mutual coupling between the elements. In this thesis, a fast simulation method for non-uniform array antennas based on mutual coupling effect will be introduced and analysed.

1.2 Background of Research History

Mutual coupling effect has been studied for about half century [22]-[24]. It exists in all array structures and represents the power interchange among elements [25]. Craeye have written a very nice review about the mutual coupling in 2011 [26]. We list the relative researches as follows.

- Minimum Scattering Antenna

A concept called Minimum Scattering Antenna was brought by Kahn in 1965 [27]. For these structures, the scattering field can be seen as zero if the antenna is open-loaded. Only very few types of antenna, such as very thin dipole and terminated waveguide, can be regarded as having the minimum scattering property. For analysing minimum scattering antenna arrays, it is enough to consider only first and second order coupling effects, otherwise increasing number of coupling orders needs to be thought about due to the huge interaction between elements in other type antenna arrays.

- Multi-port Techniques

Multi-port techniques for studying scattering field have been firstly arisen in 1973 from Harrington and Mautz [28] and they published [29], [30] in the following years where the field solution is highlighted. Those kind of N-port models offered people a new understanding of mutual coupling and multiple modes case also became available in coupling performance analysis. A. T. De Hoop wrote a paper in 1975 introducing a new analytical simulation method applicable to minimum scattering radiators, based on the network theory from Harrington and Mautz as well as properties of internal sources [31].

- Bird's Mode Matching Method (MMM) & Bailey's Interpolation

To move further, Bird brought a method calculating the mutual coupling effect between non-uniform apertures based on multi-port technique in 1979 [32]. He also gave an advanced method for rectangular apertures including a fast algorithm in 1990 [33], which is the key technique we shall use in this thesis. Furthermore, Bailey from NASA developed an interpolation method for the coupling admittance in 1996 [34], where he proposed an approximate series expression utilizing some analytical values like spacing instead of numerical integration and solving convergence, thus the process will become even more efficient.

- Initial Idea of the Thesis

C. I. Coman and I. E. Lager brought an idea of combining Bird's method and Bailey's interpolation in order to achieve an efficient strategy for analyzing the performance of non-uniform array antenna. The concept was elaborately discussed in Coman's Ph. D thesis [35]. M. Mehta [36] and L. Monlina [37] have extended the idea and tested the accuracy for Bird's and Bailey's methods with given preexisting reference data. Their approach, as such, was incomplete since it was restricted to a very small class of array antennas. The question then arises what are the steps for developing a generally applicable method for calculating the mutual coupling in non-uniform arrays consisting of aperture radiators.

1.3 Research Problem

The central problem, which is investigated in this thesis, refers to the **simulation strategy for arbitrary-placed rectangular non-uniform aperture array antennas**. The main purposes of this strategy are (1) minimizing the simulation error and (2) ensuring a wide applicability to realistic radiators for supporting real-life applications. The following five steps were then done in this thesis:

1. Study of the scattering model of non-uniform array antenna;
2. Implementation of Bird's method, development of fast algorithm and error analysis;
3. Implementation of Bailey's interpolation and error analysis;
4. Scattering matrix assembling;
5. Results processing.

Besides, an example of real non-uniform rectangular aperture array antenna will be simulated by our strategy. In order to check the capability of the method, the output will be tested by comparing with measurement results.

1.4 Outline

In this section, the outline of the whole thesis will be presented.

<u>Chapter 2</u>
In this chapter, the basic concept of mutual coupling is revised with an example of two elementary antennas. Then an overall electromagnetic model considering multi-modes was determined in terms of configuration. Several steps for obtaining feed port performance are introduced at the end.

<u>Chapter 3</u>
The mode matching method (MMM) will be discussed there. Firstly we analyze the electromagnetic field of waveguide based on Maxwell's equations and boundary condition. After that, a specific MMM from Bird is offered with the wave field expansion. The fast

algorithm for simulation will be given in the last part to deal with the extreme low computation speed of original Bird's MMM.

Chapter 4

A brief introduction of the 2D-Interpolation technique from Bailey will be done. In order to achieve best interpolation accuracy, a set of element spacing is analyzed with some proper assumptions. The case of a non-identical array is also included, where the property of 2D-Interpolation for shared aperture arrays will be tested.

Chapter 5

The chapter will focus on a practical analysis of a shared aperture design with our simulation strategy. Due to the limitation of interpolation method, a capability test will be done first for the given antenna. Then we do the overall simulation and compare the simulated results and measured results.

Chapter 6

In this last chapter the conclusions for the nine months' work will be summarized, as well as a description of its novelties. At the end, ideas for future work will be discussed.

2 Mutual Coupling

Energy flows between two elements always exist when there is a wave source outside or from themselves, which is called mutual coupling effects. The value of the energy is generally based on (*a*) radiation structure of each antenna, (*b*) relative position and (*c*) antenna orientation. [38, Chapter 8.7]

Actually, mutual coupling is a generic term for representing several mechanisms which contribute to the energy interchange. The most important reason can be found from radiation pattern, where some radiation power will be sent out of main lobe, as ideal antennas does not exist in real application. This power finally result in the change of the element far-field pattern and feed port performance. For the most general situation, mutual coupling analysis of an antenna array is difficult especially for large arrays. Although it will take enormous time and computation resources to simulate the mutual coupling, people usually have to think upon that because of its significant effect. In this section we shall first introduce the mutual effects qualitatively and then an implementation method for simulation will be given.

2.1 Coupling between Two Antennas

To demonstrate the case clearly, we only take two antenna elements A_1 and A_2 from an array, which is shown on Fig.1. The two elements are assumed to be close to each other, otherwise the interaction between them will be negligible. We assume antenna A_1 is an active unit with a power source at feed and antenna A_2 is passive. The power from the source moving along the antenna labelled as (1) will radiate in free space (2) and transmit towards antenna A_2 (3). As the result of first order coupling, the energy from A_1 generates currents on the terminal of A_2, which produce a scattered field (4) in the meantime and remaining part travel back towards the ground (5). If one takes the second iterative coupling into account, some energy of the scattered field at A_2 would travel towards A_1 which is shown as (6). The same process would occur again when two of them are all active (see Fig.2.1 (b)).

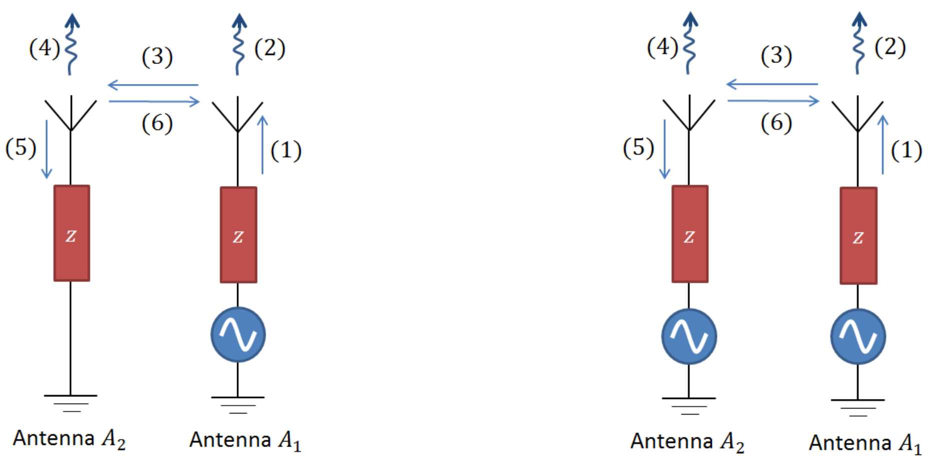

Figure 2.1 Mutual Coupling Illustration for Transmitting Mode

The wave, referred as (6) in both two cases shown on Fig.2.1, flows from A_2 to A_1 and part of it moves into the feed. Then the coupling wave will be superposed on the incident and reflected waves of antenna A_1 itself. The result is a disturbance of the radiated field. If we look at the Thévenin equivalent circuit of A_1 on Fig.2.2, the coupling wave also brings the change of current distribution on the terminal of A_1, which contributes to the antenna efficiency altering.

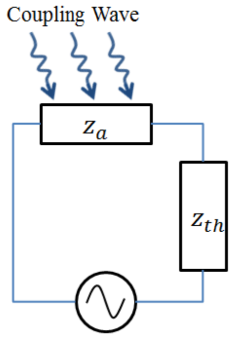

Figure 2.2 Thévenin Equivalent Circuit of Antenna A_1 with Coupling Wave

2.2 Model Analysis

To acquire the far-field pattern and feed performance, an entire coupling model is needed. The concept can be found in [39, Chapter 7.3]. The model consists of two parts: 1. Energy interchange within elements; 2. Energy interchange among all elements in free space. The analysis of single element is considered under two operational cases (active/passive) shown on Fig.2.3, where $TEM_i^{(n)}$ and $TEM_r^{(n)}$ represent the incident and reflected transverse electromagnetic (TEM) wave at the feed port of aperture n for active case. $\left[a^{(n)}\right]$ and $\left[b^{(n)}\right]$ are the backward and forward wave coefficients indicating the interaction between free space and the aperture. If we assume N modes are taken into account, the expansion of $\left[a^{(n)}\right]$ and $\left[b^{(n)}\right]$ are given in (2.1) and (2.2), in which the subscripts are labelled as the corresponding mode.

$$\left[a^{(n)}\right] = \left[a_1^{(n)}, a_2^{(n)}, a_3^{(n)}, \cdots a_N^{(n)}\right] \tag{2.1}$$

$$\left[b^{(n)}\right] = \left[b_1^{(n)}, b_2^{(n)}, b_3^{(n)}, \cdots b_N^{(n)}\right] \tag{2.2}$$

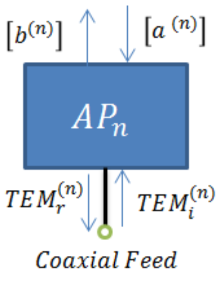

Figure 2.3 Scattering Matrix Study for Active Single Element.

There are some characteristic features needed to be collected for each elements in order to build the entire power flow network: $\left[S_{21,element}\right]$ and $\left[S_{11,element}\right]$. All of them can be obtained by simulation tools such as CST Microwave Studio® (CST). Referring to Fig. 2.3, the detailed matrix expressions for aperture n with N modes are:

$$\left[S^{(n)}_{21,element}\right] = \left[\left\langle \frac{b_1^{(n)}}{TEM_i^{(n)}} \middle| a_1^{(n)},\cdots,a_N^{(n)} = 0\right\rangle \quad \cdots \quad \left\langle \frac{b_N^{(n)}}{TEM_i^{(n)}} \middle| a_1^{(n)},\cdots,a_N^{(n)} = 0\right\rangle\right] \tag{2.3}$$

$$\left[S^{(n)}_{11,element}\right] = \left\langle \frac{TEM_r^{(n)}}{TEM_i^{(n)}} \middle| a_1^{(n)},\cdots,a_N^{(n)} = 0\right\rangle \tag{2.4}$$

On the other hand, a free space coupling matrix $[S_{air}]$ for whole array will be introduced based on Fig. 2.4 in which the matrix represents the energy interchange among all elements in free space. The expansion of $[S_{air}]$ is in (2.5)

$$[S_{air}] = \begin{bmatrix} \left[S_{air}^{(1,1)}\right] & \cdots & \left[S_{air}^{(1,M)}\right] \\ \vdots & \ddots & \vdots \\ \left[S_{air}^{(M,1)}\right] & \cdots & \left[S_{air}^{(M,M)}\right] \end{bmatrix} \tag{2.5}$$

where the $\left[S_{air}^{(i,j)}\right]$ will be expanded as (2.6). Please notice the reflected coefficients $\left[b^{(n)}\right]$ for $[S_{element}]$ is the incident component of $[S_{air}]$, and the incident coefficients $\left[a^{(n)}\right]$ for $[S_{element}]$ is the reflected component of $[S_{air}]$.

$$\left[S_{air}^{(i,j)}\right] = \begin{bmatrix} \left\langle \frac{a_1^{(i)}}{b_1^{(j)}} \middle| b_2^{(j)},\cdots,b_N^{(j)} = 0\right\rangle & \cdots & \left\langle \frac{a_1^{(i)}}{b_N^{(j)}} \middle| b_1^{(j)},\cdots,b_{N-1}^{(j)} = 0\right\rangle \\ \vdots & \ddots & \vdots \\ \left\langle \frac{a_N^{(i)}}{b_1^{(j)}} \middle| b_2^{(i)},\cdots,b_N^{(j)} = 0\right\rangle & \cdots & \left\langle \frac{a_N^{(i)}}{b_N^{(j)}} \middle| b_1^{(j)},\cdots,b_{N-1}^{(j)} = 0\right\rangle \end{bmatrix} \tag{2.6}$$

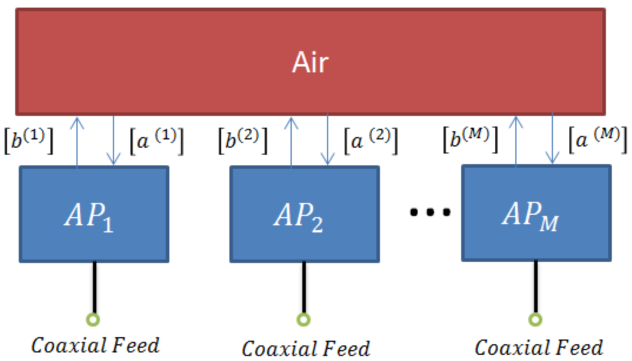

Figure 2.4 Structure Model of the Entire Array

2.3 Feed Performance Analysis

To obtain the real feed behaviour, reflection coefficient is a key character. In this thesis, three components are considered in the Γ calculation at feed port: 1. Self-reflection $\left[S_{11,active}^{(n),1}\right]$; 2. Second order coupling effect from other elements $\left[S_{11,active}^{(n),2}\right]$ (see Fig.2.1. (a) (6)); 3. Direct coupling from other elements $\left[S_{11,active}^{(n),3}\right]$ (see Fig.2.1. (b) (6)). The self-reflection can be easily acquired as $\left[S_{11,active}^{(n)}\right]$. With the concept we have introduced in previous section, the second order coupling for aperture n can be obtained by following steps:

1. $$\left[b^{(n)}\right] = TEM_i^{(n)} \cdot \left[S_{21,active}^{(n)}\right] \quad (2.7.1)$$
2. $$\left[a^{(j)}\right] = \left[b^{(n)}\right] \cdot S_{air}^{(j,n)} \quad (2.7.2)$$
3. $$\left[b^{(j)}\right] = \left[a^{(j)}\right] \cdot \left[S_{22,active}^{(j)}\right] \quad (2.7.3)$$
4. $$\left[a^{(n)}\right]=\left[b^{(j)}\right] \cdot S_{air}^{(n,j)} \quad (2.7.4)$$
5. $$TEM_r^{(n,j),2} = \left[a^{(n)}\right] \cdot \left[S_{12,active}^{(n)}\right] \quad (2.7.5)$$
6. $$\left[S_{11,active}^{(n),2}\right] = \frac{\sum_{i \neq n} TEM_r^{(n,j),2}}{TEM_i^{(n)}} \quad (2.7.6)$$

Finally, the reflection coefficient at feed on aperture n of an active array is

$$\Gamma^{(n)} = \left[S_{11,active}^{(n),1}\right] + \left[S_{11,active}^{(n),2}\right] \quad (2.8)$$

The result is acquired by considering only self-reflection and second order coupling (first order coupling is not accessed due to the principle of calculating S parameters). Once the type of array elements is not the minimum scattering antenna, a more complex algorithm is needed for the third order coupling computation.

3 Mode Matching Method

An asymptotic formula for the coupling impedance has been demonstrated firstly by Hockham [40] in 1973. He calculated the cross coupling for the TE_{10} mode for two rectangular apertures in H-plane via general scattering matrix (GSM) and compared the simulated far-field performance with the measurement. Bird gave a new asymptotic formula [32] in 1979 which was able to examine the effect of high order modes and an optimization was done for the method in 1990 [33]. In this section, Bird's concept for GSM computation of N rectangular apertures will be employed. We assume the far-field performance of an aperture is the same as the one of a same-size terminated waveguide in our thesis. Therefore, the method will be explained with a basic field analysis for waveguides in the beginning.

3.1 Electromagnetic field expansion in hollow waveguides

The field expression of inner waveguide has been investigated by many authors such as [33], [41]. In this subsection, a uniform hollow waveguide was considered in order to obtain the most general solution of the Helmholtz's equation. The solution can be seen as a superposition of modes with three different propagation types: TE, TM and TEM.

3.1.1 Field Analysis for uniform waveguides

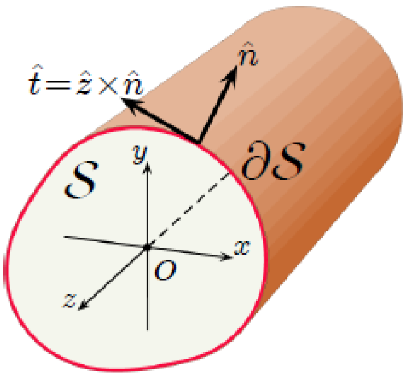

Figure 3.1 Generic uniform waveguide

A generic waveguide is depicted in Fig.3.1. It consists of a metallic boundary represented here by a cylinder filled with an isotropic dielectric.

The general field expressions derived from Maxwell's equations are given in Appendix A. However, we applied another normalized field model to solve the waveguide in our thesis where the inner field expressions of waveguide i are given by a summation of M modes as follow [41, p. 3]:

$$\boldsymbol{H}_t^i = \sum_{m=1}^{M} \left[a_m^{(i)} e^{-j\gamma_m z} - b_m^{(i)} e^{j\gamma_m z}\right] Y_m^{\frac{1}{2}} \boldsymbol{h}_m^i \tag{3.1}$$

$$\boldsymbol{E}_t^i = \sum_{m=1}^{M} \left[a_m^{(i)} e^{-j\gamma_m z} + b_m^{(i)} e^{j\gamma_m z}\right] Y_m^{-\frac{1}{2}} \boldsymbol{e}_m^i \tag{3.2}$$

where

$\boldsymbol{e}_{\boldsymbol{m}}^{\boldsymbol{i}}$ and $\boldsymbol{h}_{\boldsymbol{m}}^{\boldsymbol{i}}$ are the uniform transverse field vectors with the relation $\boldsymbol{e}_{\boldsymbol{m}}^{\boldsymbol{i}} = \boldsymbol{h}_{\boldsymbol{m}}^{\boldsymbol{i}} \times \hat{\boldsymbol{z}}$;
Y_m is the characteristic waveguide admittance of mode m and equals $Y_0\gamma_m/k$ for TE and $Y_0\epsilon_r^i k/\gamma_m$ for TM modes, ϵ_r^i is the relative electric permittivity of waveguide medium;
$\gamma_m = \sqrt{k^2 - k_{c,m}^2}$ is the wavenumber along $\hat{\boldsymbol{z}}$ for the m^{th} mode of aperture i, and $k_{c,m}$ is the cut-off wave number of mode m;
$Y_0 = \sqrt{\frac{\epsilon_0}{\mu_0}}$ is the admittance of free space;
a_m^i and b_m^i are amplitudes of the direct and reflected standard power of waveguide i with mode m.

The transverse vectors $\boldsymbol{e}_{\boldsymbol{m}}^{\boldsymbol{i}}$ and $\boldsymbol{h}_{\boldsymbol{m}}^{\boldsymbol{i}}$ can be obtained from the solution of Helmholtz's equation over the waveguide cross-section S by

$$(\nabla_t^2 + k_{c,m}^2)\phi_m = 0 \tag{3.3}$$

with the boundary conditions for different propagation mode on the edge of S :

$$\begin{aligned} \frac{\partial\phi_m}{\partial n} &= 0, \qquad \text{for TE modes} \\ \phi_m &= 0, \qquad \text{for TM modes} \end{aligned} \tag{3.4}$$

$k_{c,m}^2$ is the eigenvalue of m^{th} mode for the corresponding field and $\partial/\partial n$ is the derivative along the outward normal $\hat{\boldsymbol{n}}$ to the rim of S. ϕ_m represents the scalar eigenfunction. And the transverse vectors $\boldsymbol{e}_{\boldsymbol{m}}^{\boldsymbol{i}}$ and $\boldsymbol{h}_{\boldsymbol{m}}^{\boldsymbol{i}}$ will be evaluated once ϕ_m is solved:

$$\boldsymbol{e}_{\boldsymbol{m}}^{\boldsymbol{i}} = \begin{cases} \hat{\boldsymbol{z}} \times \nabla_t\phi_m^i, & \text{for TE modes} \\ -\nabla_t\phi_m^i, & \text{for TM modes} \end{cases} \tag{3.5}$$

$$\boldsymbol{h}_{\boldsymbol{m}}^{\boldsymbol{i}} = \widehat{\boldsymbol{z}\times} \boldsymbol{e}_{\boldsymbol{m}}^{\boldsymbol{i}} \tag{3.6}$$

where, omitting the interaction on transverse components, we have:

$$\boldsymbol{e}_{\boldsymbol{z,m}}^{\boldsymbol{i}} = \frac{k_{c,m}^2}{k}\phi_m, \qquad \text{for TM modes} \tag{3.7}$$

$$\boldsymbol{h}_{\boldsymbol{z,m}}^{\boldsymbol{i}} = \frac{k_{c,m}^2}{k}\phi_m, \qquad \text{for TE modes} \tag{3.8}$$

3.1.2 Field Expansion of Rectangular Waveguide

A depiction of a rectangular waveguide is shown on Fig. 3.2. The Helmholtz equation of the waveguide needs to be solved first in terms of different propagation mode types. Then, by specializing the formulas in Chapter 3.1.1, the vector expressions of the electric and magnetic fields will be acquired.

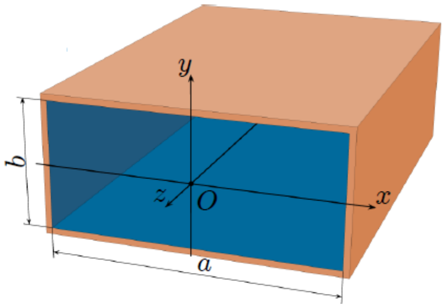

Figure 3.2 Generic rectangular waveguide

By solving the Helmholtz Eqn (3.3) with boundary condition (3.4), ϕ is acquired [42, p. 120-126):

$$\phi = \begin{cases} A_{m,n} \cos\left(\frac{m\pi x}{a}\right) \cos\left(\frac{n\pi y}{b}\right), \text{for TE modes,} & \mathrm{m, n} = 0,1,2, \ldots \\ A_{m,n} \sin\left(\frac{m\pi x}{a}\right) \sin\left(\frac{n\pi y}{b}\right), \text{for TM modes,} & \mathrm{m, n} = 1,2,3, \ldots \end{cases} \tag{3.9}$$

The index m, n represent the order of the modes for the field along horizontal and vertical directions. And the constant $A_{m,n}$ is a normalization factor for the eigenfunction, which is defined as:

$$A_{m,n} = \frac{1}{k_{c,m,n}} \sqrt{\frac{\alpha_m \alpha_n}{a\ b}} \tag{3.10}$$

where

$$\alpha_i = \begin{cases} 1, & i = 0 \\ 2, & i \neq 0 \end{cases} \tag{3.11}$$

Therefore, the normalized field expansions for rectangular waveguides with multiple modes is finally obtained by introducing (3.9) into (3.5), (3.6), (3.7) and (3.8). Tis is summarized on Table 3.1.

Table 3.1 : TE and TM modes of the rectangular waveguide		
Quantity	$TE_{m,n}$ modes	$TM_{m,n}$ modes
$\boldsymbol{\phi(x,y)}$	$A_{m,n}\cos\left(\frac{m\pi x}{a}\right)\cos\left(\frac{n\pi y}{b}\right)$	$A_{m,n}\sin\left(\frac{m\pi x}{a}\right)\sin\left(\frac{n\pi y}{b}\right)$
$\boldsymbol{e_x(x,y)}$	$-A_{m,n}\frac{n\pi}{b}\cos\left(\frac{m\pi x}{a}\right)\sin\left(\frac{n\pi y}{b}\right)$	$-A_{m,n}\frac{m\pi}{a}\cos\left(\frac{m\pi x}{a}\right)\sin\left(\frac{n\pi y}{b}\right)$
$\boldsymbol{e_y(x,y)}$	$A_{m,n}\frac{m\pi}{a}\sin\left(\frac{m\pi x}{a}\right)\cos\left(\frac{n\pi y}{b}\right)$	$-A_{m,n}\frac{n\pi}{b}\sin\left(\frac{m\pi x}{a}\right)\cos\left(\frac{n\pi y}{b}\right)$
$\boldsymbol{e_z(x,y)}$	0	$A_{m,n}\frac{\boldsymbol{k_{c,m,n}^2}}{k}\sin\left(\frac{m\pi x}{a}\right)\cos\left(\frac{n\pi y}{b}\right)$
$\boldsymbol{h_x(x,y)}$	$-A_{m,n}\frac{m\pi}{a}\sin\left(\frac{m\pi x}{a}\right)\cos\left(\frac{n\pi y}{b}\right)$	$A_{m,n}\frac{n\pi}{b}\sin\left(\frac{m\pi x}{a}\right)\cos\left(\frac{n\pi y}{b}\right)$
$\boldsymbol{h_y(x,y)}$	$-A_{m,n}\frac{n\pi}{b}\cos\left(\frac{m\pi x}{a}\right)\sin\left(\frac{n\pi y}{b}\right)$	$-A_{m,n}\frac{m\pi}{a}\cos\left(\frac{m\pi x}{a}\right)\sin\left(\frac{n\pi y}{b}\right)$
$\boldsymbol{h_z(x,y)}$	$A_{m,n}\frac{\boldsymbol{k_{c,m,n}^2}}{k}\cos\left(\frac{m\pi x}{a}\right)\cos\left(\frac{n\pi y}{b}\right)$	0
$\boldsymbol{A_{m,n}}$	$\frac{1}{k_{c,m,n}}\sqrt{\frac{\alpha_m\alpha_n}{a\,b}}$	
$\boldsymbol{k_{c,m,n}}$	$\sqrt{\left(\frac{m\pi}{a}\right)^2+\left(\frac{n\pi}{b}\right)^2}$	

3.2 Algorithm of MMM

In order to acquire the coupling effect between two apertures, firstly the transverse magnetic field at $\boldsymbol{R}$ from the reference $\boldsymbol{R'}$ was calculated in (3.12) and (3.13) by the Green function with equivalent magnetic current M' [43, Chapter 18], where the M' indicated the tangential electric field of the aperture by applying equivalence theory.

$$M' = \hat{\mathbf{z}} \times 2\boldsymbol{E_t}(R',0) \tag{3.12}$$

$$\boldsymbol{H_t}(R) = jk_0\xi_0\left(1+\frac{\nabla_t\nabla_t}{k_0^2}\right)\cdot\hat{\mathbf{z}}\times\int_{-\infty}^{\infty}\int dS\, M'G(|\boldsymbol{R}-\boldsymbol{R'}|) \tag{3.13}$$

where $G(R) = \frac{e^{-jk_0R}}{4\pi R}$ is the scalar free space Green's function and ∇_t is the transverse gradient operator. $k_0 = \frac{2\pi}{\lambda_0}$ is the wave number in free space.

Here we take an assumption for the far-field model, where the field expression at $R - R' = 0^+$ is same for the field at $R - R' = 0^-$. In this way, the far-field in Fig.3.3 can be represented by a combination of the field inside waveguide, free space phase shift, and attenuation caused by radiation distance.

$$\boldsymbol{H_t}(R',0^-) = \boldsymbol{H_t}(R',0^+) \tag{3.14}$$

$$\boldsymbol{H_t}(R',R) = \boldsymbol{H_t}(R',0^+) * \frac{e^{-jk_0R}}{R} \tag{3.15}$$

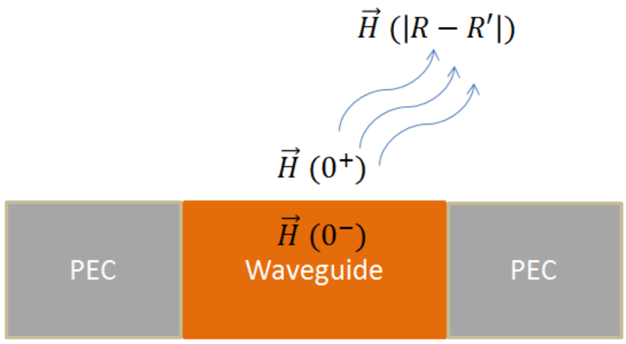

Figure 3.3 Field Illustration for Single Aperture

By introducing eqn (3.1) and eqn (3.2) into eqn(3.13), all possible trial aperture field solutions can be solved with (3.16). A Galerkin procedure is applied to figure out the coupling admittance [33] between $\boldsymbol{H_t}$ and $\boldsymbol{E_t}$ for two apertures.

$$N_m^i B_m^i Y_m^{i\,\frac{1}{2}} = \sum_n 2jk_0\xi_0 Y_n^{j-\frac{1}{2}} A_n^j \iint_{D_i} dS\, \boldsymbol{h_m^i} \cdot \left(1 + \frac{\nabla_t \nabla_t}{k_0^2}\right) \cdot \iint_{D_j} dS'\, \boldsymbol{h_n^j} G(|R - R'|) \tag{3.16}$$

where

$$\begin{aligned} A_n^j &= a_n^j + b_n^j \\ B_m^i &= a_m^i - b_m^i \end{aligned} \tag{3.17}$$

and

$$N_m^i = \iint_{D_i} \boldsymbol{h_m^i} \cdot \boldsymbol{h_m^i}\, dS \tag{3.18}$$

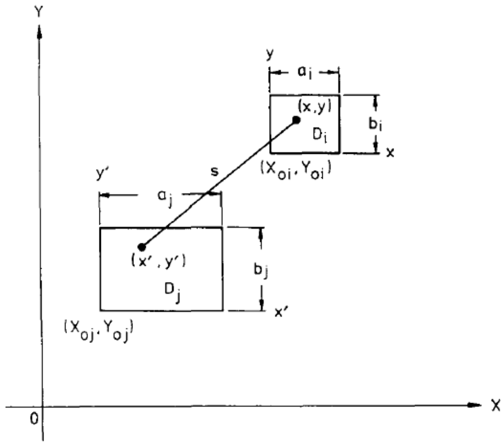

Figure 3.4 Differently Sized Rectangular Waveguide-ends on the Ground Plane

After an equation transformation with Einstein notation, Eqn (3.16) can be rewritten as

$$B_m^i = Y_{m,n}^{i,j} A_n^j \tag{3.19}$$

and

$$Y_{m,n}^{i,j} = \frac{2jk_0\xi_0}{\sqrt{Y_n^j\, Y_m^i}} \iint_{D_i} dS\, \boldsymbol{h_m^i} \cdot (1 + \frac{\nabla_t \nabla_t}{k_0^2}) \cdot \iint_{D_j} dS'\, \boldsymbol{h_n^j} G(|R - R'|) \tag{3.20}$$

The expression describes the coupling between mode m of waveguide i and mode n of waveguide j.

By simplification, we finally have the general expression for coupling admittance as:

$$Y_{m,n}^{i,j} = \frac{2jk_0Y_0}{N_m\sqrt{Y_n^j\, Y_m^i}} \iint_{D_i} dS\, \boldsymbol{\Psi_m} \cdot \iint_{D_j} dS'\, \boldsymbol{\Psi_n} G(|R - R'|) \tag{3.21}$$

where $\boldsymbol{\Psi_m} = \boldsymbol{h_m} + \gamma_m \boldsymbol{h_{zm}}/k$, which is a vector that represents the combination of transverse and normal magnetic field components $\boldsymbol{h_m}$ and $\boldsymbol{h_{zm}}$; N_m is $\boldsymbol{h_m^i} \cdot \boldsymbol{h_m^i}$ integrated over the aperture D_i and equals 2 in this case.

By applying the field expressions for rectangular waveguides in Table 1 with (3.21), we finally have the coupling admittance formula for our method:

$$Y_{m,n}^{i,j} = 2\pi^2 jk_0Y_0 \cdot \alpha_{m,n}\alpha_{m',n'}(c_xI_x + c_yI_y - c_zI_z) \tag{3.22}$$

where

$$\begin{matrix} I_x \\ I_y \\ I_z \end{matrix} = \iint\limits_{D_i} dS \iint\limits_{D_j} dS'\, G(|R - R'|) * \begin{matrix} sin \\ cos \\ cos \end{matrix}\left(\frac{m\pi x}{a_i}\right) \begin{matrix} cos \\ sin \\ cos \end{matrix}\left(\frac{n\pi y}{b_i}\right) \begin{matrix} sin \\ cos \\ cos \end{matrix}\left(\frac{m'\pi x'}{a_j}\right) \begin{matrix} cos \\ sin \\ cos \end{matrix}\left(\frac{n'\pi y'}{b_j}\right) \tag{3.23}$$

and

$$\alpha_{mn} = \sqrt{\frac{2\epsilon_{0m}\epsilon_{0n}}{a_ib_iY_{mn}k_{c,mn}^2}} \tag{3.24}$$

c_x, c_y and c_z are as listed in Table 2 with four possible coupling combination types.

TABLE2
Coefficients of Admittance Formula

Coupling Type	c_x	c_y	c_z
$\boldsymbol{TE_{m,n} \leftrightarrow TE_{m',n'}}$	$\frac{mm'}{a_ia_j}$	$\frac{nn'}{b_ib_j}$	$\left(\frac{k_{c,m,n}k_{c,m',n'}}{\pi k}\right)^2$
$\boldsymbol{TE_{m,n} \leftrightarrow TM_{m',n'}}$	$\frac{-mn'}{a_ib_j}$	$\frac{nm'}{b_ia_j}$	0
$\boldsymbol{TM_{m,n} \leftrightarrow TE_{m',n'}}$	$\frac{-nm'}{b_ia_j}$	$\frac{mn'}{a_ib_j}$	0
$\boldsymbol{TM_{m,n} \leftrightarrow TM_{m',n'}}$	$\frac{nn'}{b_ib_j}$	$\frac{mm'}{a_ia_j}$	0

3.3 Fast Calculation of MMM Method

Although the formula for coupling admittance is derived, computation time will be enormously long due to four iterative integral loops. Therefore, a fast calculation method for Bird's MMM is given in this subsection which brings down the computation time to several seconds.

The basic idea of the method is reducing the number of integrals [44, Chapter 6]. In practical cases (see Fig.3.5), Eqn (3.23) will be rewritten as (3.25), where we assume $x_0 = 0, y_0 = 0$ and $\Delta_x = x_0' - x_0$, $\Delta_y = y_0' - y_0$.

$$\begin{matrix} I_x \\ I_y \\ I_z \end{matrix} = \iint_{D_i} dS \iint_{D_j} dS' \, G(x - x', y - y') \\ * \begin{matrix} \sin \\ \cos \\ \cos \end{matrix} \left(\frac{m\pi x}{a_i}\right) \begin{matrix} \cos \\ \sin \\ \cos \end{matrix} \left(\frac{n\pi y}{b_i}\right) \begin{matrix} \sin \\ \cos \\ \cos \end{matrix} \left(\frac{m'\pi(x' - \Delta_x)}{a_j}\right) \begin{matrix} \cos \\ \sin \\ \cos \end{matrix} \left(\frac{n'\pi(y' - \Delta_y)}{b_j}\right) \tag{3.25}$$

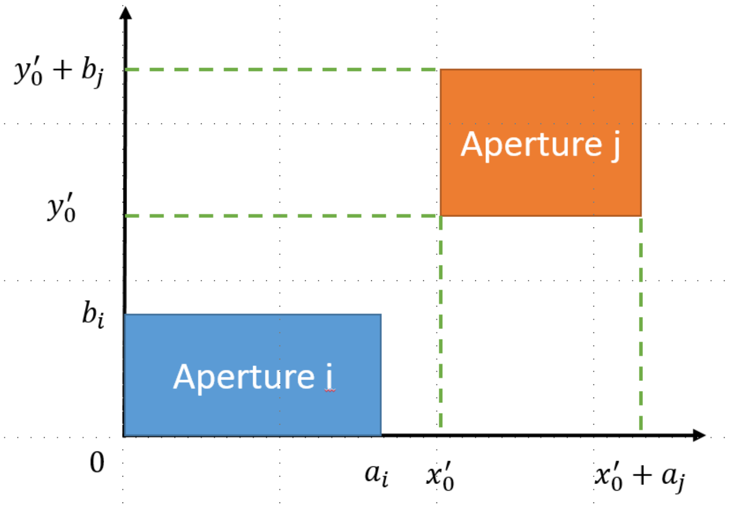

Figure 3.5 Illustration of Positions of Two Aperture

Based on (3.25), the equation can be finally transformed into (3.26), with the detailed derivation being given in Appendix B.

$$\begin{matrix} I_x \\ I_y \\ I_z \end{matrix} = \begin{matrix} I_-^1(x, x', a_i, a_j, dx) I_+^2(y, y', b_i, b_j, dy) \\ I_+^1(x, x', a_i, a_j, dx) I_-^2(y, y', b_i, b_j, dy) \\ I_+^1(x, x', a_i, a_j, dx) I_+^2(y, y', b_i, b_j, dy) \end{matrix} \tag{3.26}$$

where

$$I_\pm^1 = \frac{1}{2}\int_{-a_j}^{a_i} L_\pm(\sigma, V_A^1, U_A^1, a_i, a_j) d\sigma - \frac{1}{2}\int_{-a_j}^{0} L_\pm(\sigma, V_B^1, U_B^1, a_i, a_j) d\sigma \\ - \frac{1}{2}\int_{a_i - a_j}^{a_i} L_\pm(\sigma, V_C^1, U_C^1, a_i, a_j) d\sigma \tag{3.27}$$

$$I_{\pm}^{2} = \frac{1}{2}\int_{-b_j}^{b_i} G(\sigma-\Delta_x,\lambda-\Delta_y)L_{\pm}(\lambda,V_A^2,U_A^2,b_i,b_j)d\lambda - \frac{1}{2}\int_{-b_j}^{0} G(\sigma-\Delta_x,\lambda-\Delta_y)\,L_{\pm}(\lambda,V_B^2,U_B^2,b_i,b_j)d\lambda - \frac{1}{2}\int_{b_i-b_j}^{b_i} G(\sigma-\Delta_x,\lambda-\Delta_y)\,L_{\pm}(\lambda,V_C^2,U_C^2,b_i,b_j)d\lambda \tag{3.28}$$

and

$$L_{\pm}(\sigma,V_A,U_A,a_i,a_j) = \left\{\pm sinc\left[\frac{\pi}{2}\left(\frac{m}{a_i}+\frac{m'}{a_j}\right)U_A\right]cos\left[\frac{\pi}{2}\left(\frac{m}{a_i}(\sigma+V_A)+\frac{m'}{a_j}(-\sigma+V_A)\right)\right] + sinc\left[\frac{\pi}{2}\left(\frac{m}{a_i}-\frac{m'}{a_j}\right)U_A\right]cos\left[\frac{\pi}{2}\left(\frac{m}{a_i}(\sigma+V_A)+\frac{m'}{a_j}(\sigma-V_A)\right)\right]\right\} \tag{3.29}$$

with

$V_A^1 = \sigma + a_j$	$V_B^1 = 0$	$V_C^1 = a_i + a_j$
$U_A^1 = a_j$	$U_B^1 = -\sigma$	$U_C^1 = a_j - a_i + \sigma$
$V_A^2 = \lambda + b_j$	$V_B^2 = 0$	$V_C^2 = b_i + b_j$
$U_A^2 = b_j$	$U_B^2 = -\lambda$	$U_C^2 = b_j - b_i + \lambda$

3.4 Simulation Test and Error Analysis

Simulations of the apertures were processed both in CST and Matlab. Reflection coefficients of TE_{10} in different coupling cases are illustrated in following figures. For the geometry of the tested apertures, the length of the long edge $a = 15.7mm$, the short edge $b = 7.7mm$ and filled material is vacuum.

3.4.1 Self-coupling

The reflection coefficient $|S_{11,TE_{10}}|$ with different simulated mode numbers for a single element is shown on Fig. 3.6. We observe the coupling admittance for TE_{10} has a slight variation with the increasing number of simulated modes. The reason is due to the limited mode number, where contributions of modes from $M+1$ to ∞ will be added to the first M modes if only M modes are considered.

Taking example of mode m, the imaginary part of the propagation constant γ_m refers to the attenuation constant α_m, which grows when higher evanescent modes (larger than m) are considered. Therefore, the coupling effect of a mode decreases with the increase of mode order. That explains why the difference tends to be smaller when number of simulated modes increases. Besides, it is noted that there exists some distorted value of $|S_{11}|$ above 0 dB at the cut-off of TE_{10} mode. The phenomenon is attributed to the representation of a limited mode number when we calculate the field expression numerically at this particular frequency [45].

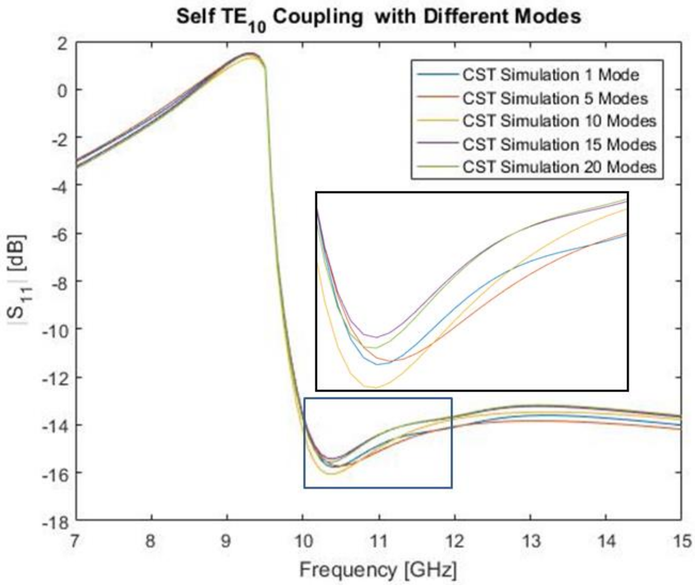

Figure 3.6 Plot of $|S_{11,TE_{10}}|$ in CST with different number of simulated modes

The simulation and error analysis for TE_{10} are shown on Fig. 3.7 (a) (b) (c) considering different number of simulated modes. The observation frequency was taken from 7 GHz to 15 GHz with 100 equidistant points. Besides, error rate calculated by (3.30) decreases with larger number of considered modes.

$$Error_{TE_{10}} = \left| \frac{S_{11,TE_{10},CST} - S_{11,TE_{10},MMM}}{S_{11,TE_{10},CST}} \right| \tag{3.30}$$

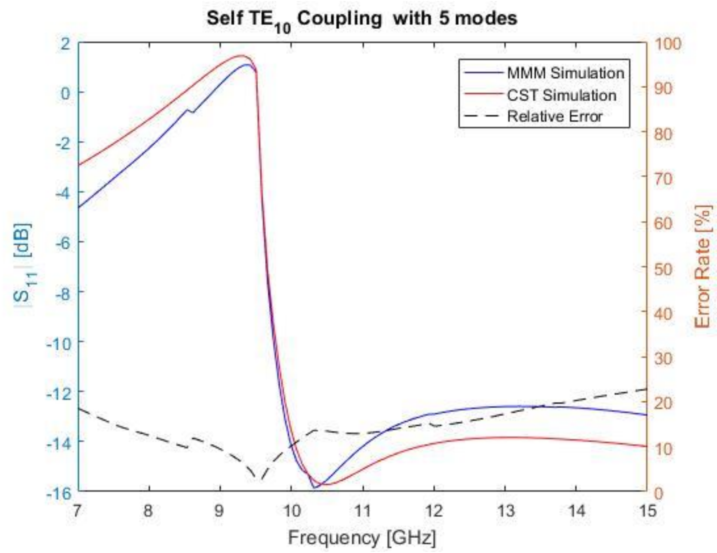

(a)

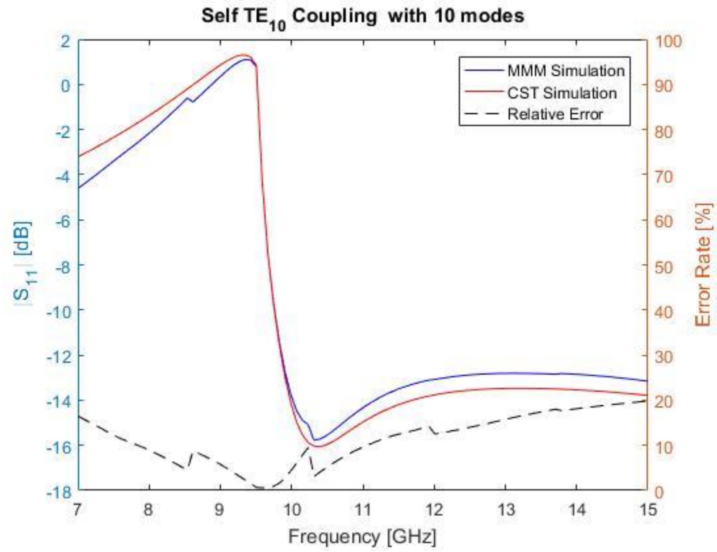

(b)

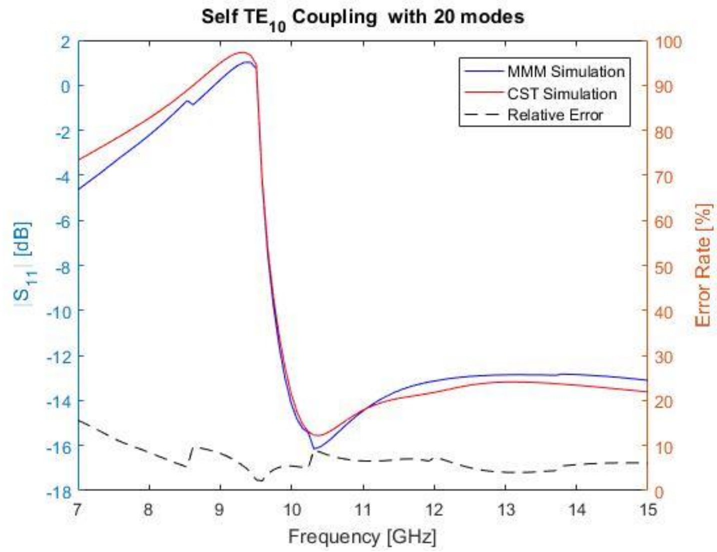

(c)

Figure 3.7 Simulation and Error Plot of $|S_{11,TE_{10}}|$ with Different Number of Analysed Modes. (a) 5 Modes; (b) 10 Modes; (c) 20 Modes.

3.4.2 Coupling of Two Identical Apertures

Several cases were investigated to evaluate the numerical implementation for mutual coupling of two identical apertures in this section. The configuration is illustrated in Fig.8 where $d_1 = 20mm$ and $d_2 = 15mm$. For all the four subfigures, there are dramatic changes occurring at $9.7\ GHz$ which indicate the cut-off frequency of TE_{10} mode of the aperture. As the radiated field of TE_{10} only exists in the E-plane, the coupling effect for the layout in Fig.3.8 (a) is less active compared with the layout in Fig.3.8 (b). The result from Fig.8 (c) and Fig.8 (d) are similar due to the similar strength of co-polarization in (c) and cross-polarization in (d).

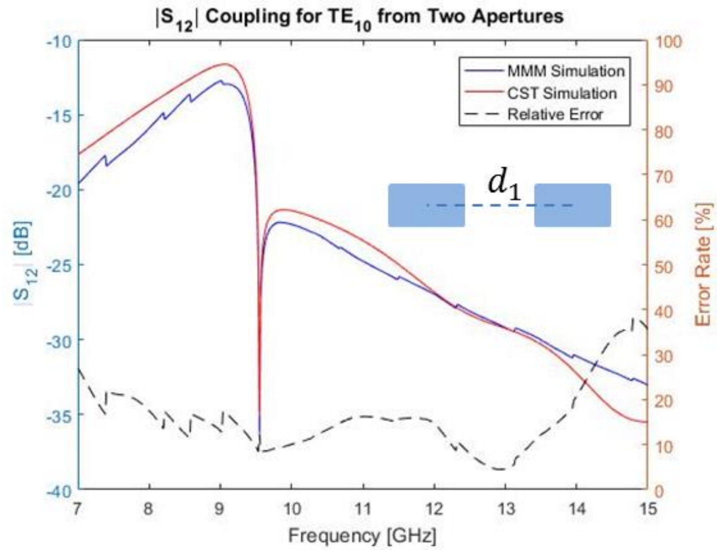
$|S_{12}|$ Coupling for TE_{10} from Two Apertures
MMM Simulation
CST Simulation
Relative Error
d_1
$|S_{12}|$ [dB]
Error Rate [%]
Frequency [GHz]

(a)

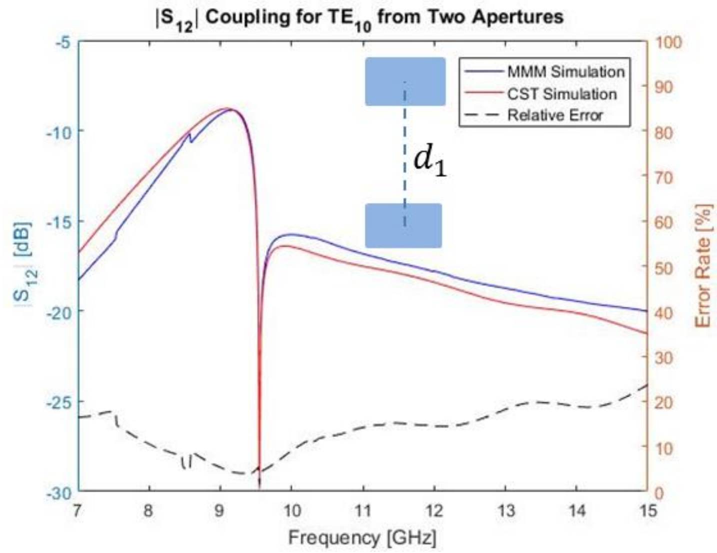
$|S_{12}|$ Coupling for TE_{10} from Two Apertures
MMM Simulation
CST Simulation
Relative Error
d_1
$|S_{12}|$ [dB]
Error Rate [%]
Frequency [GHz]

(b)

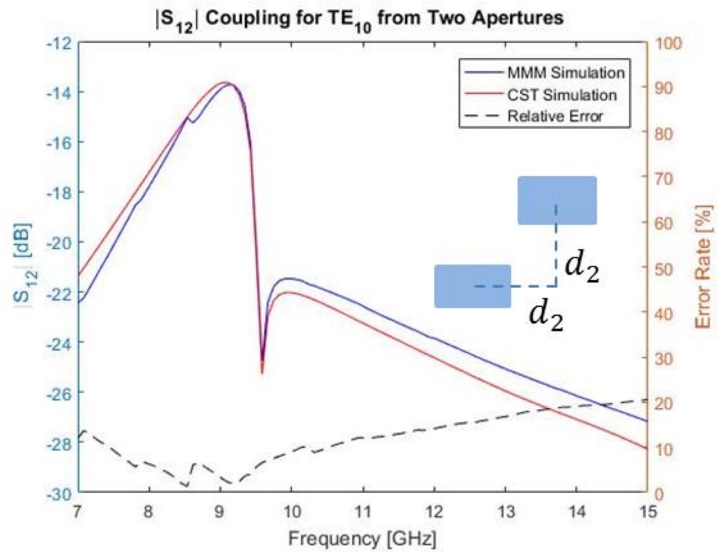
$|S_{12}|$ Coupling for TE_{10} from Two Apertures
MMM Simulation
CST Simulation
Relative Error
d_2
d_2
$|S_{12}|$ [dB]
Error Rate [%]
Frequency [GHz]

(c)

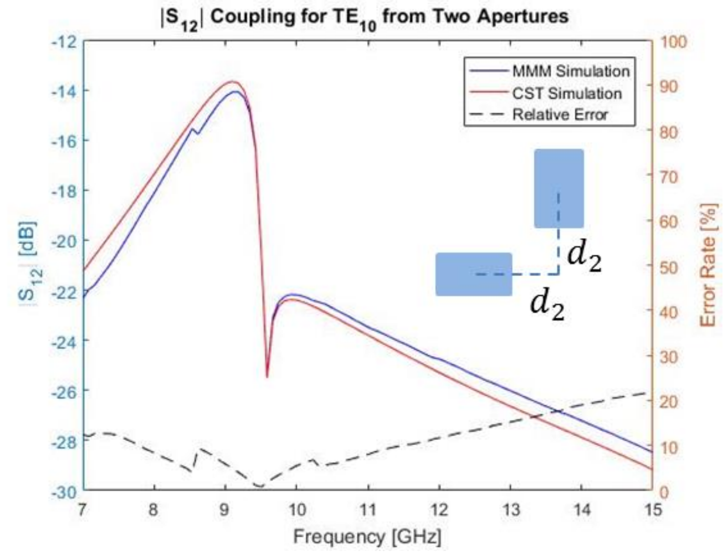

(d)

Figure 3.8 Simulation and Error Plot of $\left|S_{12,TE_{10}}\right|$ with Different Configuration (a) Same orientation on X-axis; (b) Same orientation on Y-axis; (c) Same orientation on diagonal; (d) Orthogonal orientation on diagonal.

3.4.3 Coupling of Two Different Apertures

In this subchapter, a new aperture is introduced to demonstrate the accuracy of the method for elements in different size. The new aperture is a square and has $a' = 22.8mm$ as the length of sides. It is positioned right above and diagonally to the reference aperture as shown in Fig.3.9. Compared with the results on Fig. 3.8, the error in amplitude increases when two different radiation models are applied. An even larger phase error occurs when the two apertures are set diagonally in Fig.3.9 (b). In our point of view, the obvious difference between the two simulation outputs mainly comes from the discrepant understanding of coupling between our approach and CST designers, for which we need time to figure it out.

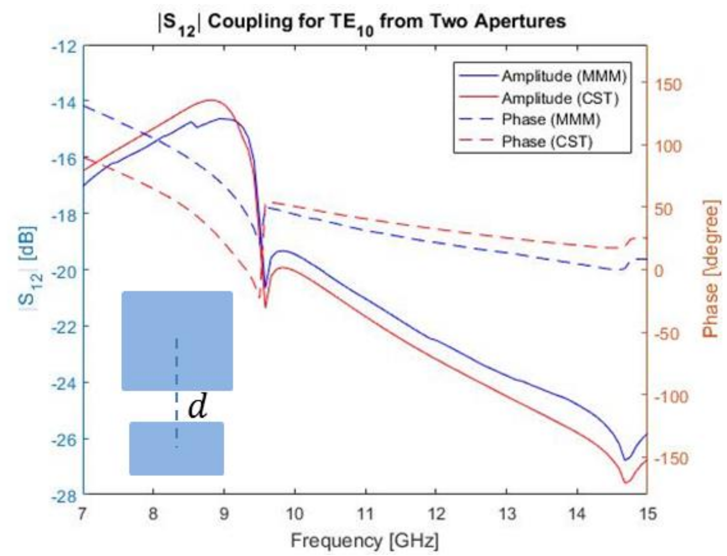

(a)

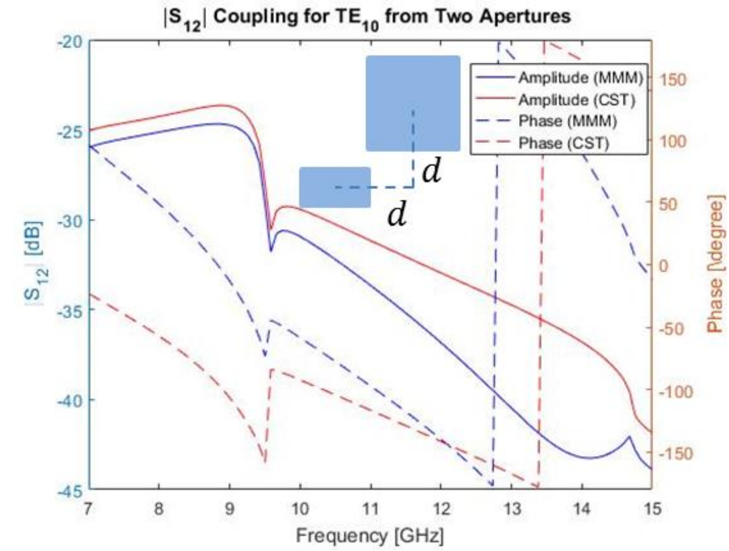

(b)

Figure 3.9 Simulation and Error Plot of $\left|S_{12,TE_{10}}\right|$ with Different Configuration (a) Same Orientation (b) Orthogonal Orientation

4 2-D Interpolation of Coupling Admittance

4.1 Introduction of 2-D Interpolation Technique

The Floquet method is a good far-field solution for uniform array antennas. However, once coupling effect, multiple modes or non-identical elements are considered, the Floquet theory cannot be used anymore and people usually apply numerical methods to solve the problem. It is obvious that the numerical computations take time when accounting for coupling effects between all the modes in all the apertures within a large array. Therefore, we applied Bailey's 2-D Interpolation [34] here as a fast method calculating mutual coupling admittance.

The main idea of 2-D Interpolation is calculating coupling admittance for two arbitrary modes between two arbitrary apertures based on several known coupling cases. Christian Coman offered a complete formula for interpolation based on the originnal expression of Bailey by adding a new component [35]. Manjula Mehta then checked the accuracy of the new formula via simulations [46]. We implemented the new formula here:

$$
\begin{aligned}
Y_{mn,m'n'} = \Bigg\{ & \left[A_1 \left(\frac{1}{kr'}\right) + A_2 \left(\frac{1}{kr'}\right)^2 + A_3 \left(\frac{1}{kr'}\right)^3 \right] \cos^2 \phi \\
& + \left[A_4 \left(\frac{1}{kr'}\right) + A_5 \left(\frac{1}{kr'}\right)^2 + A_6 \left(\frac{1}{kr'}\right)^3 \right] \sin^2 \phi \\
& + \left[A_7 \left(\frac{1}{kr'}\right) + A_8 \left(\frac{1}{kr'}\right)^2 + A_9 \left(\frac{1}{kr'}\right)^3 \right] \sin^2 (2\phi) \Bigg\} \exp(-jkr')
\end{aligned} \tag{4.1}
$$

where r' is the centre distance between two apertures and ϕ refers to the geometric angle from the sample aperture to the reference aperture.

As can be seen in (4.1), In order to acquire the interpolation coefficients from A_1 to A_9, nine coupling cases need to be considered for the nine unknown values. Therefore, nine basis apertures and one reference aperture on the origin are applied for the calculation. Besides, the solution processes for the coefficients can be simplified by selecting three basis apertures along x-axis ($\phi = 0$) and three along y-axis ($\phi = \pi/2$). As for the last three basis apertures, they can be set at anywhere in principle except two axis, while we put them at the direction of $\phi = \pi/4$ in the design.

4.2 Error Analysis

As it has been explained, for the purpose of acquiring nine interpolation coefficients, nine basis apertures need to be determined. The S matrix between basis apertures and reference aperture will be calculated by the MMM method, which has been introduced in Section 2.

However, the position of the nine basis apertures cannot be set arbitrarily, otherwise a large error may occur with some improper cases. By looking back to the Eqn (4.1), apparently the coefficients A_3, A_6 and A_9 with factor $\left(\frac{1}{kr'}\right)^3$ refer to the "near-field" contribution. Similarly, A_2, A_5 and A_8 represent the "intermediate field" and A_1,A_4 and A_7 are the parameters on behalf of "far-field". In this way, for the "near-field region", "intermediate field region" and "far-field region", we shall set three basis apertures in each region. The "near-field region" refers the case two apertures are very close to each other and the "far-field region" indicates the situation when the coupling is really small but still non-negligible (in our case threshold is -60 dB for admittance). The "Intermediate field region" is somewhere in between the two regions.

4.2.1 Model of Error Analysis

We only consider identical rectangular apertures in this analysis. In order to acquire all the coefficients for (4.1), we took apart the equation into 3 parts as (4.2), (4.3) and (4.4) and solved them separately. The calculation of $Y^2_{mn,m'n'}$ calculation is made here (all waveguides are same in both size and orientation with $a = 9.7\ mm$, $b = 4.3\ mm$ and $f = 16\ GHz$).

$$Y^1_{mn,m'n'} = \left[A_1\left(\frac{1}{kr'}\right) + A_2\left(\frac{1}{kr'}\right)^2 + A_3\left(\frac{1}{kr'}\right)^3\right]\cos^2\phi\exp(-jkr') \tag{4.2}$$

$$Y^2_{mn,m'n'} = \left[A_4\left(\frac{1}{kr'}\right) + A_5\left(\frac{1}{kr'}\right)^2 + A_6\left(\frac{1}{kr'}\right)^3\right]\sin^2\phi\exp(-jkr') \tag{4.3}$$

$$Y^3_{mn,m'n'} = \left[A_7\left(\frac{1}{kr'}\right) + A_8\left(\frac{1}{kr'}\right)^2 + A_9\left(\frac{1}{kr'}\right)^3\right]\sin^2(2\phi)\exp(-jkr') \tag{4.4}$$

Obviously, when $Y^2_{mn,m'n'}$ needs to be calculated, all the basis aperture centres lay on y-axis as shown below on Fig. 4.1, where d_1,d_2 and d_3 are the centre distance between basis apertures and the reference aperture.

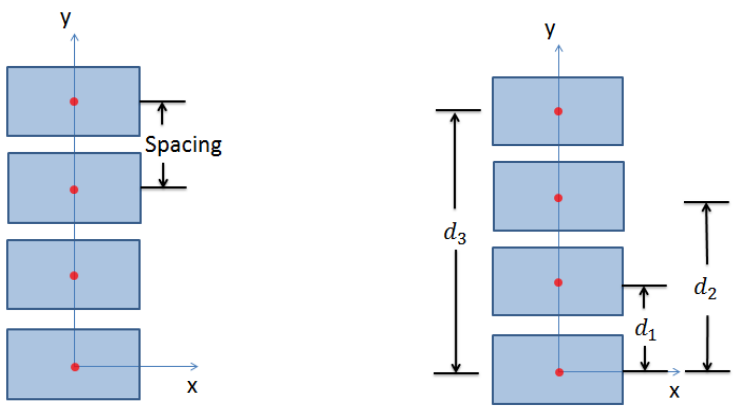

Figure 4.1 Illustration of $Y^2_{mn,m'n'}$ Computation

By applying 2-D Interpolation, three general admittance matrixes (GAM) were calculated firstly with d_1,d_2 and d_3 by using MMM method as the basis. Then the A matrix was calculated by (4.5):

$$A_{mn,m'n'} = \begin{bmatrix} A_{4,mn,m'n'} \\ A_{5,mn,m'n'} \\ A_{6,mn,m'n'} \end{bmatrix} = R^{-1} * \begin{bmatrix} Y^2_{mn,m'n'}(d_1)\exp(jkd_1) \\ Y^2_{mn,m'n'}(d_2)\exp(jkd_2) \\ Y^2_{mn,m'n'}(d_3)\exp(jkd_3) \end{bmatrix} \tag{4.5}$$

where

$$R = \begin{bmatrix} (kd_1)^{-1} & (kd_1)^{-2} & (kd_1)^{-3} \\ (kd_2)^{-1} & (kd_2)^{-2} & (kd_2)^{-3} \\ (kd_3)^{-1} & (kd_3)^{-2} & (kd_3)^{-3} \end{bmatrix} \tag{4.6}$$

Similarly, A_1, A_2 and A_3 will be acquired by implementing the above steps with basis apertures lying on x-axis. And we can also obtain the value of A_7,A_8 and A_9 using the similar linear procedures with known coefficients from $A_1$to A_6.

By calculating the mutual coupling admittance between test aperture and reference aperture, the error can be determined. However, the error varies a lot with the position shift of the test aperture. In order to obtain a general value of error, a group of test apertures are applied and a normalized Gaussian weight function is implemented, where expectation $\mu = \sqrt{a^2 + b^2}$ and standard deviation $\sigma = \lambda - \sqrt{a^2 + b^2}$. For example of $Y^2_{mn,m'n'}$, the formula of general error is (4.7) and $y' \in [y_1, y_2]$.

$$Error_{avg} = \sum_{y'=y_1}^{y_2} \frac{\left|Y^{2,interpolated}_{mn,m'n'}(d_1, d_2, d_3, y') - Y^{2,ref}_{mn,m'n'}(y')\right|}{\left|Y^{2,ref}_{mn,m'n'}(y')\right|} Gaussian(\mu, \sigma, y') \tag{4.7}$$

where

$$Gaussian(\mu, \sigma, y') = \frac{\frac{1}{\sqrt{2\pi\sigma^2}} e^{-\frac{(y'-\mu)^2}{2\sigma^2}}}{\sum_{y'=y_1}^{y_2} \frac{1}{\sqrt{2\pi\sigma^2}} e^{-\frac{(y'-\mu)^2}{2\sigma^2}}} \tag{4.8}$$

The practical position domain of the test apertures in our design is roughly determined with several steps. Here we still take the case in Fig. 4.1 for example:

1. Generally we determine d_3 as 3λ where the coupling admittance is smaller than 60 dB. For some specific case where the value of d_3 needs to be studied, I take $d_3 \in [2.5\lambda, 4\lambda]$.
2. By using the far-field boundary formula (4.9), a larger virtual receiver size D will be calculated. With the D, the upper limit of near-filed boundary which refers to d_1 can be acquired with Eqn (4.10). As for d_2, representing the intermediate field region, can be determined as (4.11).

$$d_{3i} \geq \frac{2D^2}{\lambda} \tag{4.9}$$

$$d_{1i} \leq 0.62\sqrt{\frac{D^3}{\lambda}} \tag{4.10}$$

$$0.62\sqrt{\frac{D^3}{\lambda}} \le d_{2i} \le \frac{2D^2}{\lambda} \tag{4.11}$$

3. The position selection of test apertures is based on practical application, which means no overlapping with the central aperture. Therefore the test apertures in the design were set along axis for analysis of $Y^1_{mn,m'n'}$ and $Y^2_{mn,m'n'}$, and $\phi_0 \in [15°, 30°, 45°, 60°, 75°, 90°]$ and $\rho \in [\sqrt{a^2+b^2}, 3\lambda]$ for $Y^3_{mn,m'n'}$ analysis.

4.2.2 Positions of Basis Apertures for Same Orientation

In order to have a clear view of the method, the structure for interpolation between same orientation apertures is illustrated in Fig 4.2.

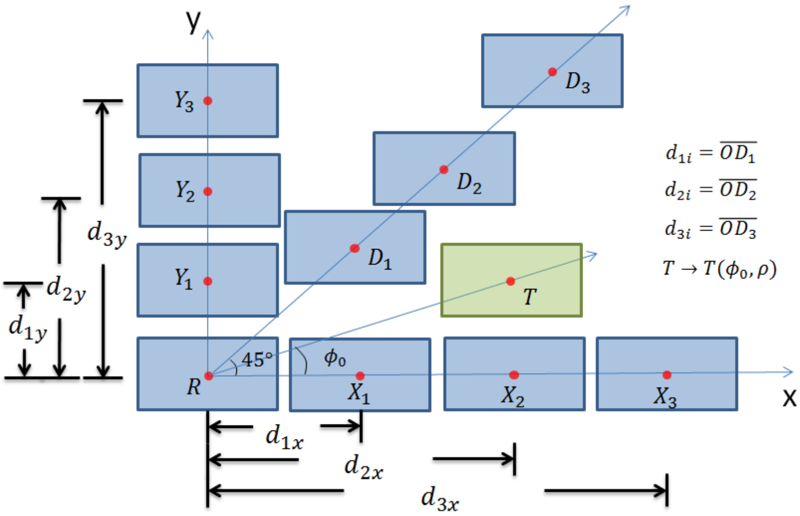

Figure 4.2 Implementation of Interpolation with Same Orientation

4.2.2.1 Choice of aperture located along axis

The interpolation along y-axis is firstly considered. According to the assumption, there are four variables affecting the value of average error, which is very hard to do the variable optimization simultaneously. Hence we fixed the value of d_{3y} as $[2.5\lambda, 3\lambda, 3.5\lambda, 4\lambda]$ which represents the far field distance and did little impact on the change of near-field admittance. Our simulation results for the main mode (TE_{10}) are shown on Fig. 4.3. Obviously, the figure is highlighted at $d_{1y} = 0.233\lambda$ which indicates an area for low error rate.

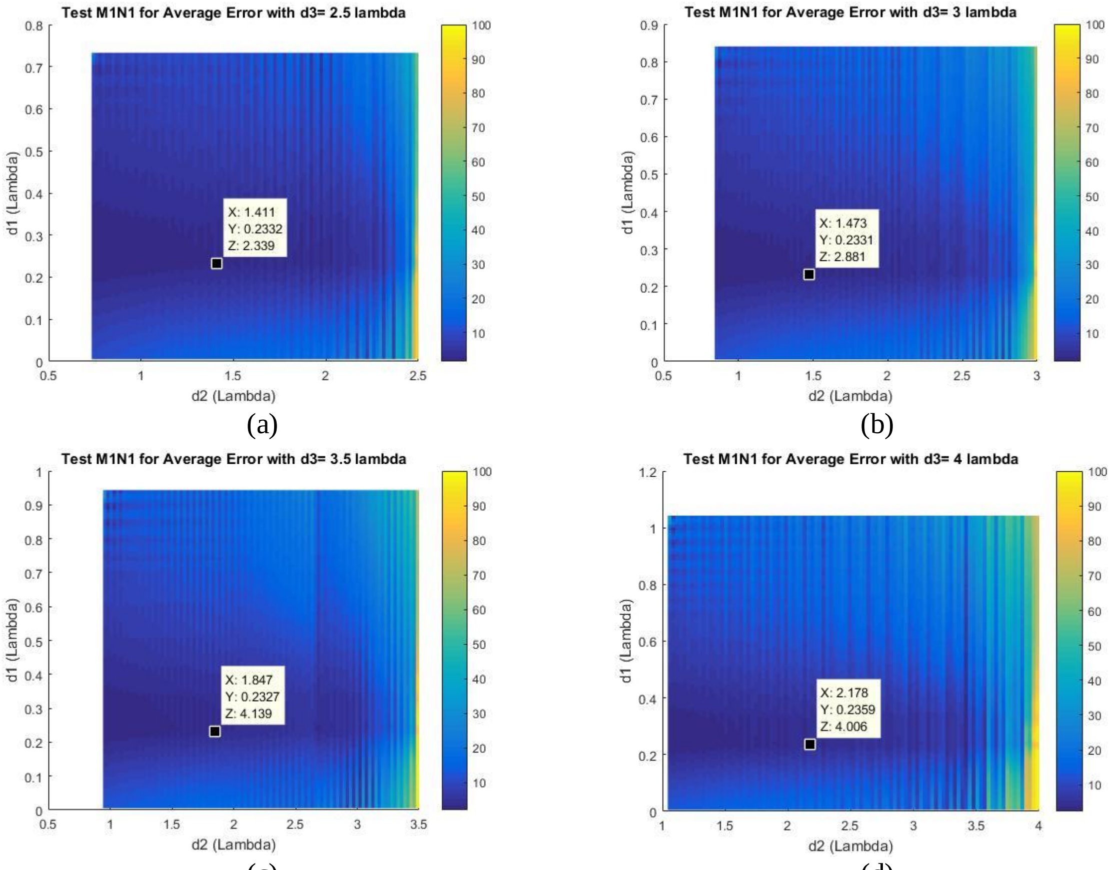

Figure 4.3 General Error Plot for TE_{10} with Different d_{3y}. (a) $d_{3y} = 2.5\lambda$; (b) $d_{3y} = 3.5\lambda$; (c) $d_{3y} = 3.5\lambda$; (d) $d_{3y} = 4\lambda$.

With the fixed d_{1y} value, the minimal error plot with d_{3y} and d_{2y} was made. We illustrate the error distribution in the figure below (see Fig. 4.4). Due to the fact that coupling effect decreases with increasing spacing, the second reference position d_{2y} tends to be smaller which contributes to a more accurate approximation of near-region coupling effect. On the contrary, the far-field coupling factor has little impact on the output and thus the selection of d_{3y} has a large-scale tolerance. The best choice of d_{2y} and d_3y can be easily obtained and our selection is $d_{1y} = 0.233\lambda \approx b, d_{2y} = 0.84\lambda$ and $d_{3y} = 3.0\lambda$.

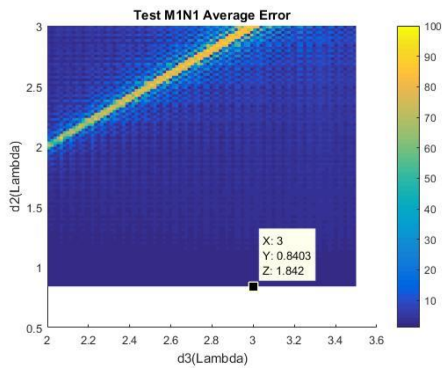

Figure 4.4 General Error Plot for TE_{10} with Fixed $d_{1y} = b$

However, this is one single solution to the problem. As can be seen in the figure above, multiple choices for the combination of d_{2y} and d_{3y} exist and they all offer a low error rate. Therefore, in order to find out the inner relationship between appropriate (d_{2y}, d_{3y}) and apertures, several simulations are done. For the selection of d_{1y} and d_{2y}, we tested it with fixed d_{3y} with 3λ in different working frequency (single mode propagation), aperture size and modes. All the results indicates $d_{1y} = b$ for the minimum error. This phenomenon helps reduce the complexity in the overall analysis.

In principle, the interpolation coefficients are supposed to be recalculated for every pair of coupling modes, which may result in enormous computation time. We tested the tolerance of the main mode spacing by applying that in higher mode coupling calculation. The errors of three strongest coupling mode pairs ($TE_{10} \leftrightarrow TE_{10}$, $-28.5dB$ at 1λ; $TE_{10} \leftrightarrow TM_{11}$, $-34.5\ dB$ at 1λ; $TM_{11} \leftrightarrow TM_{11}$, -44.4$dB$ at 1λ) are shown in Fig. 4.5, where $TE_{10} \leftrightarrow TE_{10}$ is 3.4%, $TE_{10} \leftrightarrow TM_{11}$has 6.3% and $TM_{11} \leftrightarrow TM_{11}$ reaches 31.6%. Considering the amplitude of the coupling admittance, I think the interpolation spacing of main mode can be applied to calculate the coupling for higher modes with acceptable error.

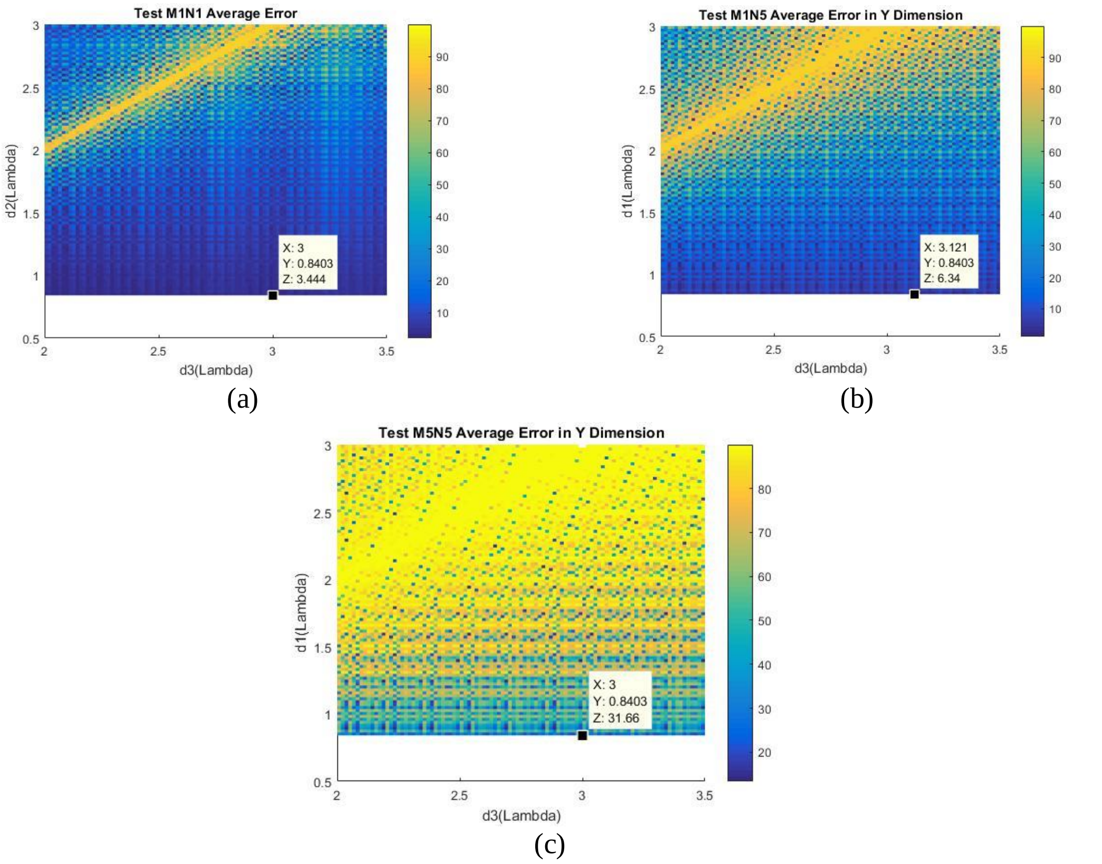

Figure 4.5 General Error Plot for Different Mode Type (a) $TE_{10} \leftrightarrow TE_{10}$; (b) $TE_{10} \leftrightarrow TM_{11}$; (c) $TM_{11} \leftrightarrow TM_{11}$

The analysis for interpolation along x-axis is also considered in a similar way. As the result, our decision for minimum error for $Y^1_{mn,m'n'}$ is $d_{x1} = a$, $d_{x2} = 0.84\lambda$ and $d_{x3} = 3\lambda$.

4.2.2.2 *Choice of aperture located on diagonal direction* $(45°)$

For observing the relationship between d_{1i} and d_{2i} with minimum error, $d_{3i} = 3.5\lambda$ is applied for this simulation. Admittance error is computed based on variable d_{1i} and d_{2i} and shown in Fig. 4.6. For all the plots, relatively low and acceptable error rate can be easily achieved by a board-scale combination of d_{1i} and d_{2i}. Then, as the choice, we take $d_{1i} = 0.3263\lambda \approx \sqrt{2}b$ which results in low error rate (Actually, best choice of d_{1i} should be seen as $\sqrt{2}Min[a,b]$ in general case).

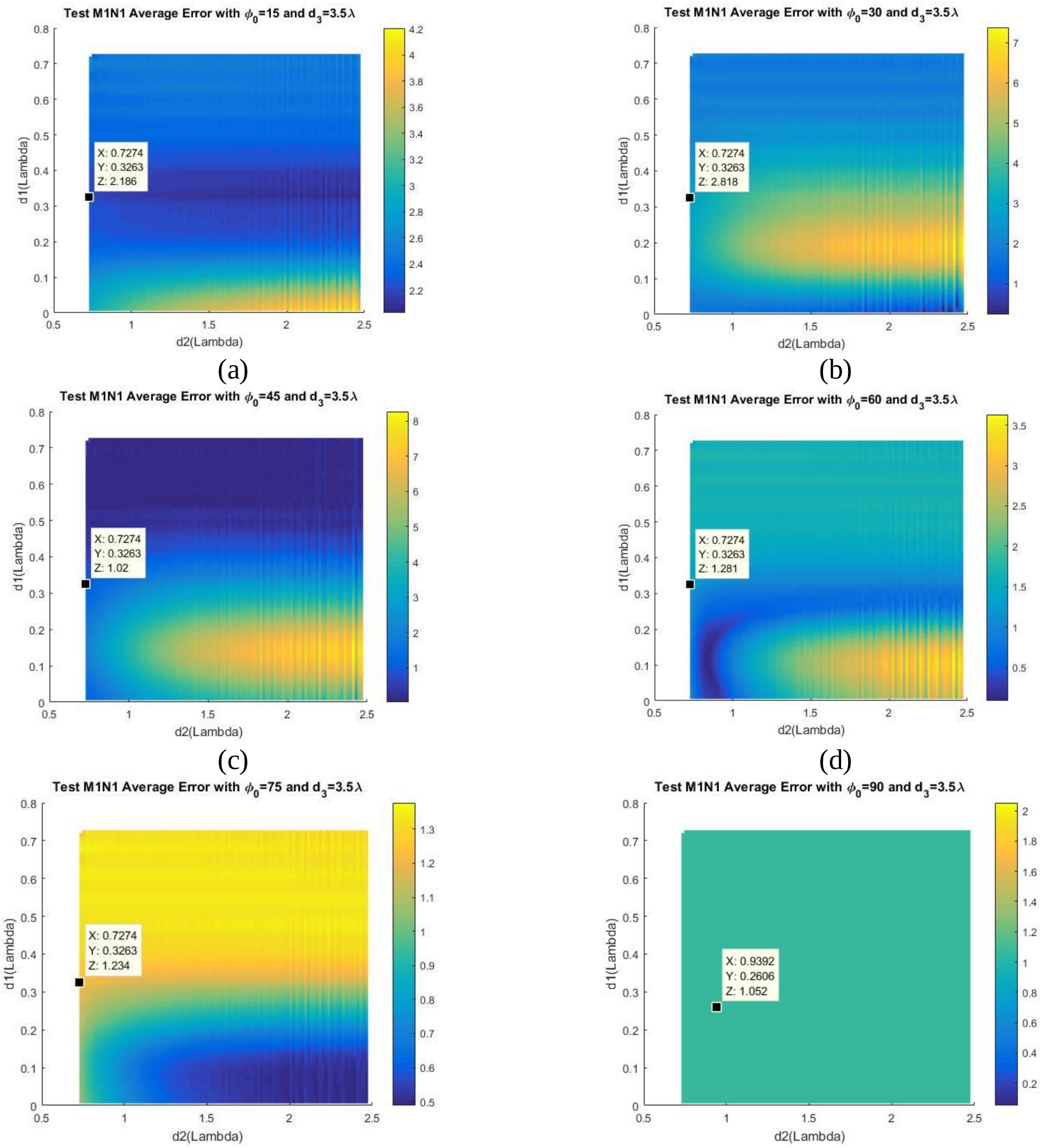

(e) (f)

Figure 4.6 General Error Plot for TE_{10} with Different ϕ and $d_{3i} = 3.5\lambda$. (a) $\phi = 15°$; (b) $\phi = 30°$; (c) $\phi = 45°$; (d) $\phi = 60°$; (e) $\phi = 75°$; (f) $\phi = 90°$.

Based on the assumption of $d_{1i} = \sqrt{2}b$, we start analysing the relation between d_{2i} and d_{3i} for minimum admittance error, where the variation of the far-field distance d_{3i} was taken into account. In the test, we did the simulation with $d_{3x} = 3\lambda, d_{3y} = 3\lambda$ and d_{3i} varies from 2.5λ

to 4λ. The results are shown in Fig. 4.7 where it still offers a large scale for selection and we took $d_{1i} = \sqrt{2}b$, $d_{2i} = 1\lambda$ and $d_{3i} = 3\lambda$.

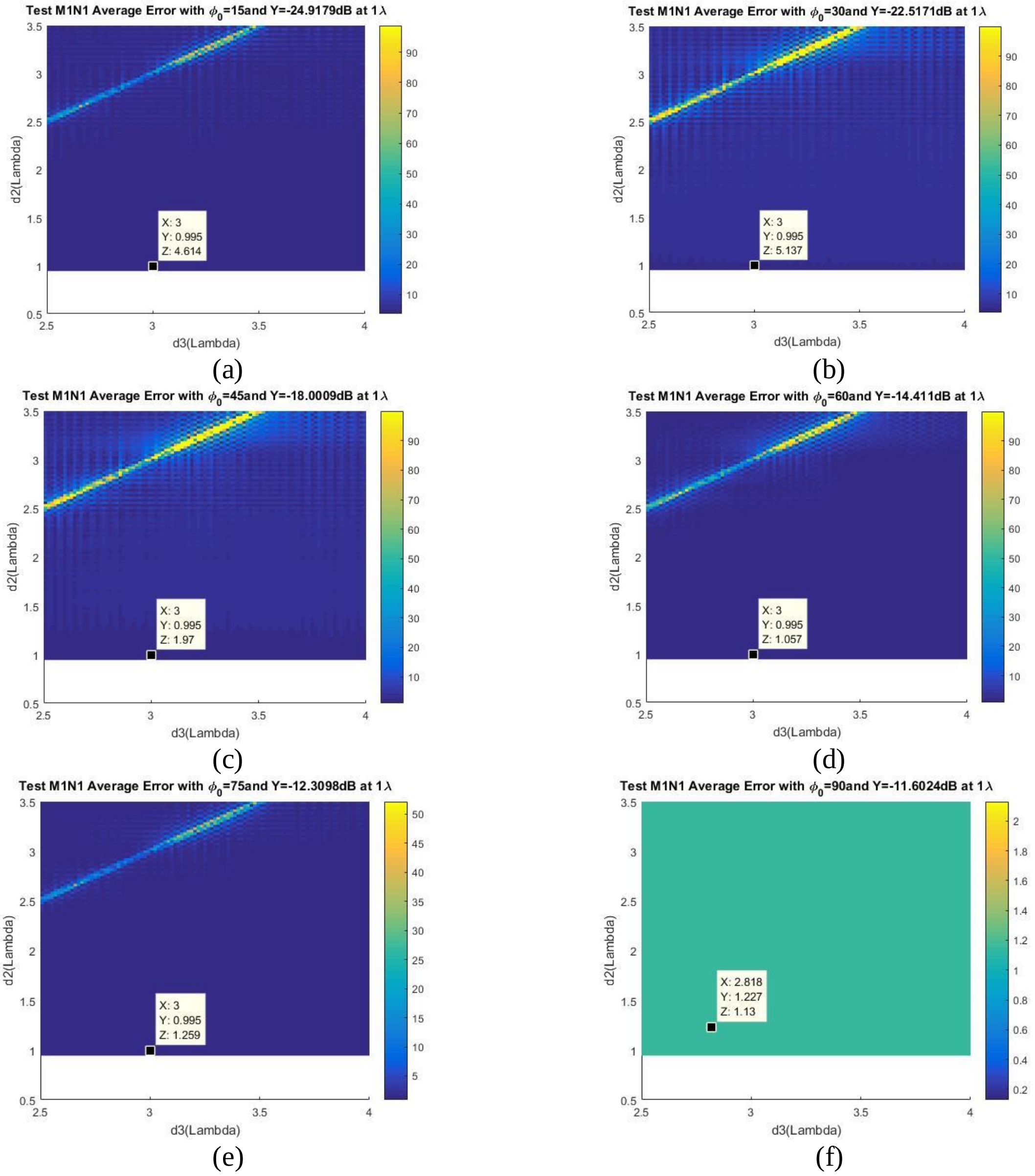

Figure 4.7 General Error Plot for TE_{10} with Different ϕ and $d_{1i} = \sqrt{2}b$. (a) $\phi = 15°$; (b) $\phi = 30°$; (c) $\phi = 45°$; (d) $\phi = 60°$; (e) $\phi = 75°$; (f) $\phi = 90°$.

4.2.3 Positions of Basis Apertures for Orthogonal Orientation

Another interpolation case with orthogonal apertures is analysed in this section. The corresponding structure is shown on Fig. 4.8. Procedures for interpolation coefficients are the same as what we have done before, where basis apertures along y direction, x direction and bisector will be considered. However, the accuracy of the method becomes worst in this case because zero coupling is achieved for the basis apertures along y-axis and x-axis, where the relative error is quite large according to (4.8). The detail steps will be introduced in the following subsections.

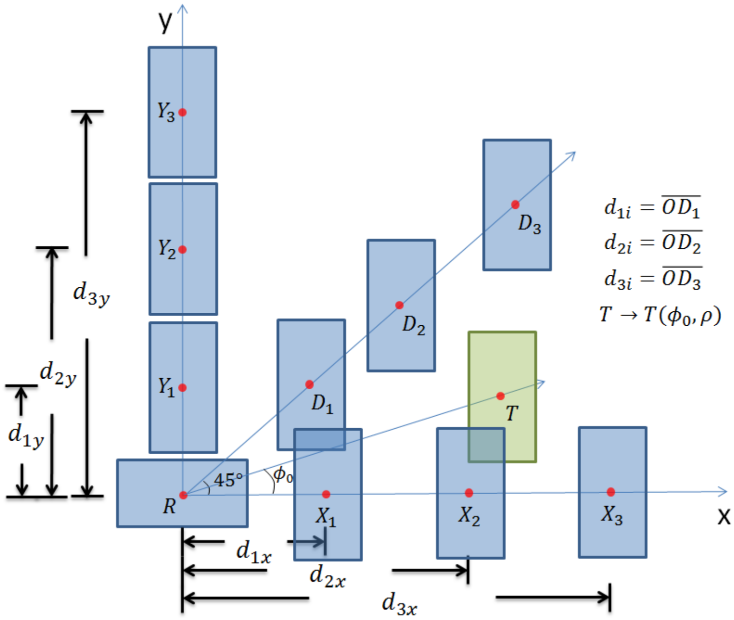

Figure 4.8 Implementation of Interpolation with Same Orientation

4.2.3.1 Choice of aperture located along axis

Coupling admittance in y-direction was considered first. Since it was not appropriate to analysis main mode ($TE_{10} \leftrightarrow TE_{10}$) due to the zero coupling, interpolation spacing will be tested based on some higher mode combination with significant coupling effect. With fixed $d_{3y} = 3.5\lambda$, Here are the simulation results for several modes (Fig. 4.9. $TE_{10} \leftrightarrow TE_{01}$ for (a), $TE_{20} \leftrightarrow TE_{10}$ for (b), $TE_{01} \leftrightarrow TE_{10}$ for (c), $TE_{01} \leftrightarrow TE_{20}$ for (d)). There is a highlighted area for all plots at $d_{1y} = 0.375\lambda \approx \frac{1}{2}(a + b)$ which refers to the low error rate.

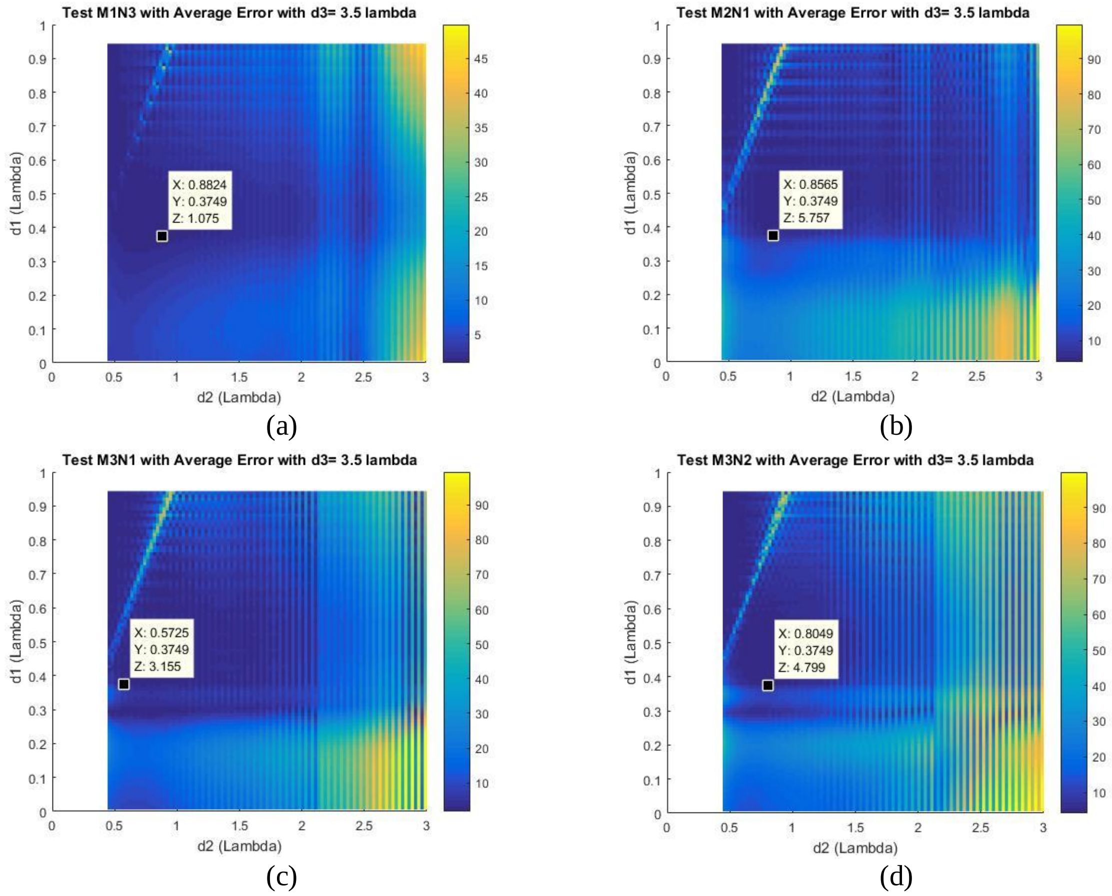

Figure 4.9 General Error Plot for Higher modes with Fixed d_{3y}. (a) $TE_{10} \leftrightarrow TE_{01}$; (b) $TE_{20} \leftrightarrow TE_{10}$; (c)), $TE_{01} \leftrightarrow TE_{10}$; (d) $TE_{01} \leftrightarrow TE_{20}$.

With the fixed d_{1y}, we made the error plot with d_{3y} and d_{2y}. Meanwhile, the Gaussian weight function was applied again in this procedure with $u = \frac{1}{2}(a+b)$ and $\sigma = \lambda - u$. We only put the error distribution for $TE_{10} \leftrightarrow TE_{01}$ (22.1 dB coupling at 1λ central distance) on Fig. 4.10, while other modes has relatively small coupling strength (less than -33 dB at 1λ central distance) which is negligible. The choice we took for d_{2y} and d_{3y} is: $d_{2y} = 1\lambda$ and $d_{3y} = 2.8\lambda$.

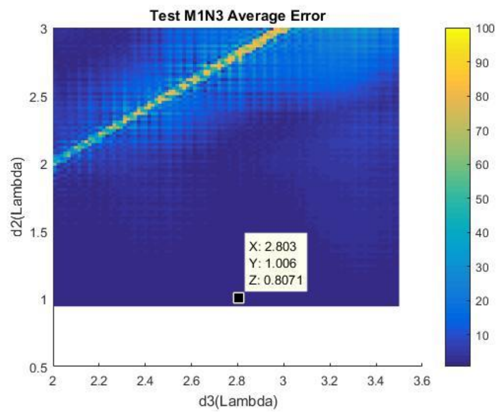

Figure 4.10 General Error Plot for $TE_{10} \leftrightarrow TE_{01}$ with Fixed $d_{1y} = \frac{1}{2}(a+b)$

4.2.3.2 Choice of aperture located on diagonal direction (45°)

To observe the relationship between d_{1i} and d_{2i} with minimum error, $d_{3i} = 3.5\lambda$ and $d_{3y} = d_{3x} = 2.8\lambda$ were applied for this simulation. The result for $TE_{11} \leftrightarrow TE_{11}$(the strongest coupling) is shown on Fig. 4.11. For all the plots, relatively low and acceptable error rate can be easily achieved by some combinations of d_{1i} and d_{2i}. Then, as the choice, we took $d_{1i} = 0.4\lambda \approx \sqrt{2}(0.5a + b)$ (actually should be $\frac{\sqrt{2}}{2}(a + b + \min[a, b])$.

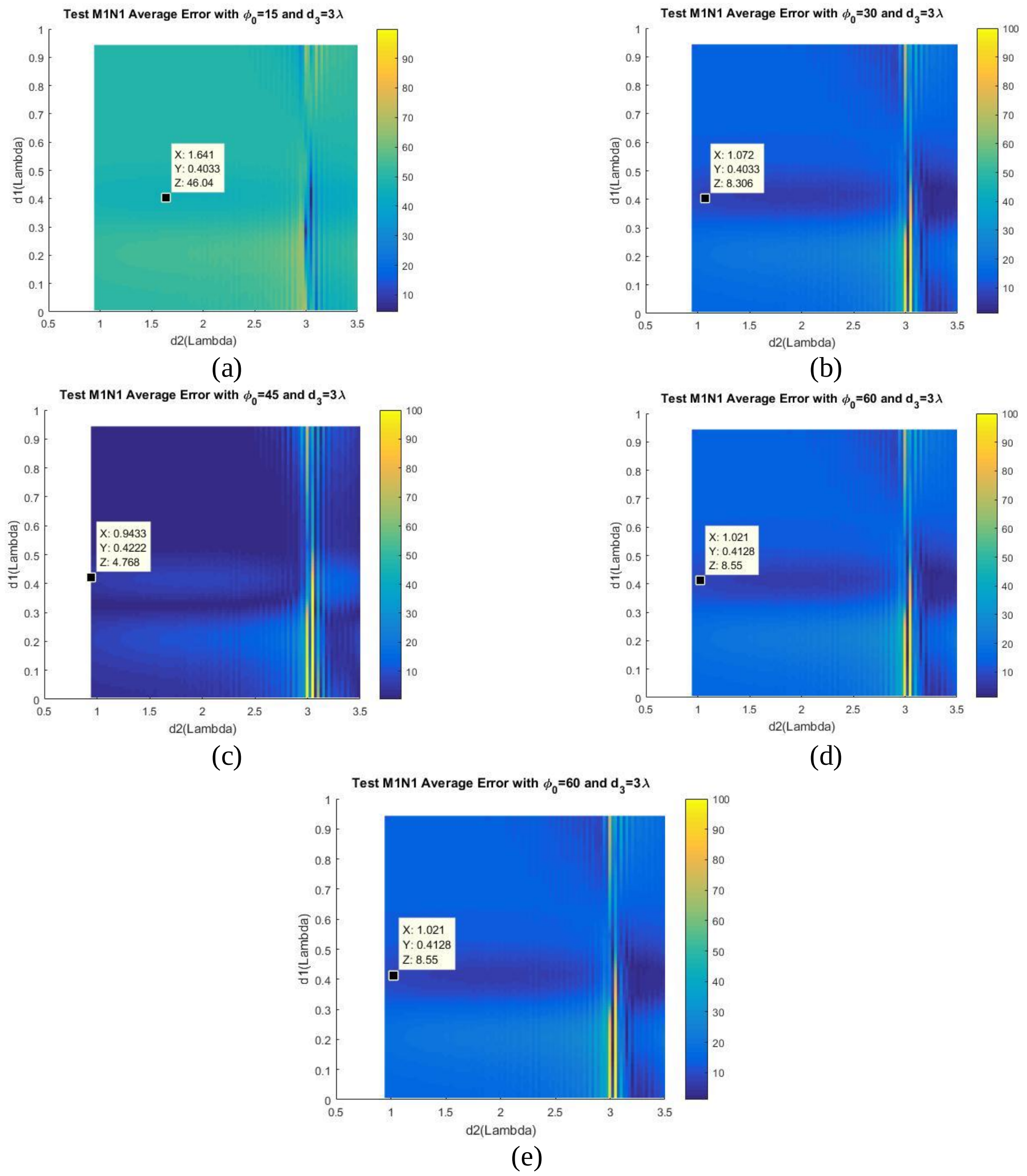

Figure 4.11 General Error Plot for $TE_{11} \leftrightarrow TE_{11}$ with Different ϕ and $d_{3i} = 3.5\lambda$. (a) $\phi = 15°$; (b) $\phi = 30°$; (c) $\phi = 45°$; (d) $\phi = 60°$; (e) $\phi = 75°$.

Based on the assumption of $d_{1i} = \sqrt{2}(0.5a + b)$, we started analysing the relation between d_{2i} and d_{3i} for minimum admittance error, where the small impact from the variation of far-field distance d_{3i} was tested. The simulation with $d_{3x} = 3\lambda, d_{3y} = 3\lambda$ and d_{3i} varies from 2.5λ to 4λ was done and the results are shown on Fig. 4.12. It still offers a large scale for selection and I took $d_{1i} = \sqrt{2}(0.5a + b)$, $d_{2i} = 1\lambda$ and $d_{3i} = 3\lambda$ as the spacing parameters in the end. However, due to the high error rate out of $[30°, 60°]$ scale, we recommend MMM for calculating the coupling admittance for orthogonal apertures instead of interpolation method.

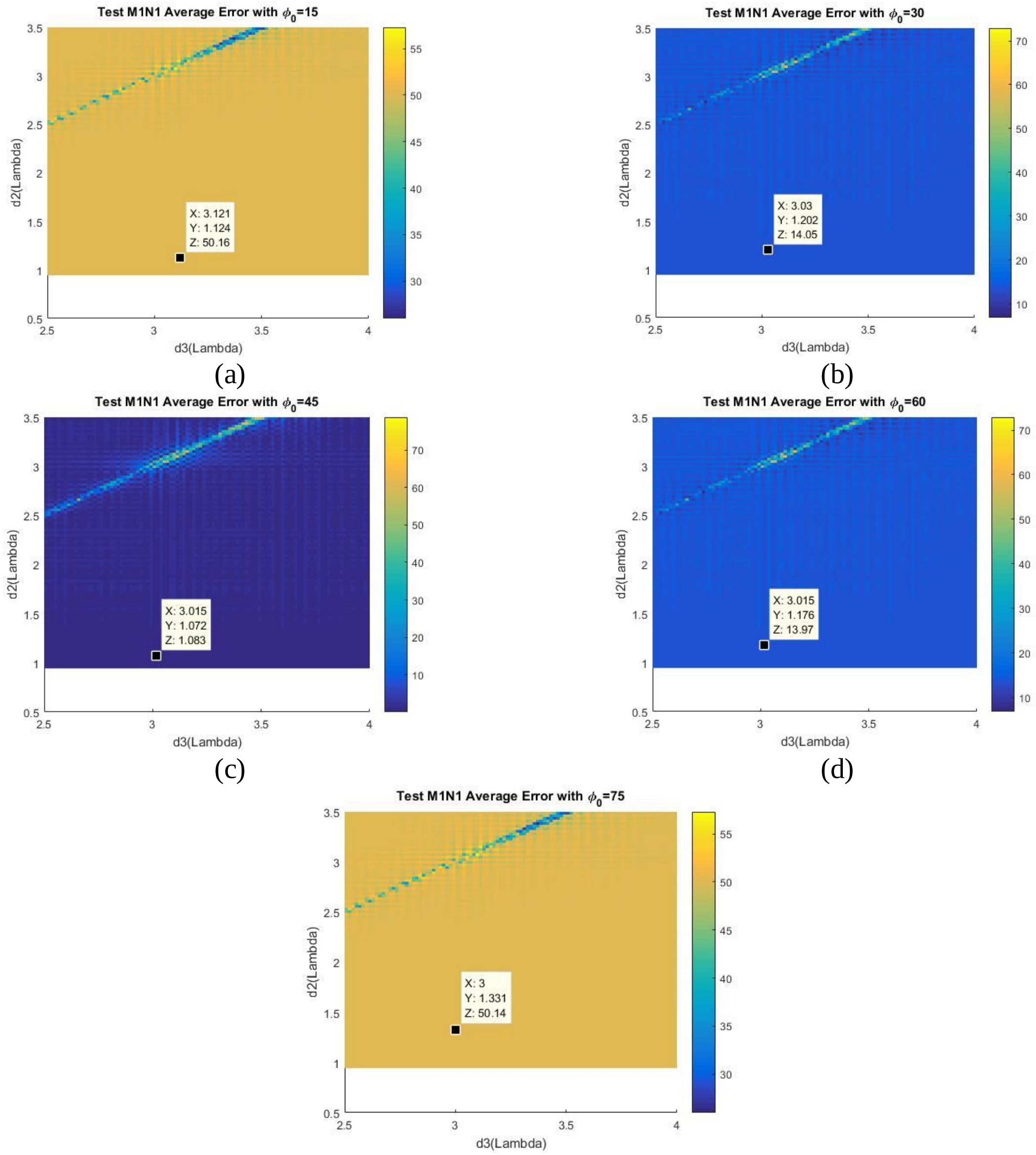

(e)

Figure 4.12 General Error Plot for $TE_{10} \leftrightarrow TE_{10}$ with Different ϕ and $d_{3i} = 3.5\lambda$. (a) $\phi = 15°$; (b) $\phi = 30°$; (c) $\phi = 45°$; (d) $\phi = 60°$; (e) $\phi = 75°$.

4.2.4 Summary of Preferred Spacing

In summary, we listed the minimum-error positions of nine basis apertures for two coupling types in the two tables, where the reference aperture is located at origin with length a along x-axis and length b along y-axis. For the case of same orientation, the preferred spacing is in Table 3.1 referring to Fig. 3.2. And Table 3.2 gives the preferred spacing for coupling of orthogonal apertures.

Table 3.1 Preferred Spacing of Apertures in Same Orientation		
$\boldsymbol{d_{1x} = a}$	$d_{2x} = 0.84\lambda$	$d_{3x} = 3\lambda$
$\boldsymbol{d_{1y} = b}$	$d_{2y} = 0.84\lambda$	$d_{3y} = 3\lambda$
$\boldsymbol{d_{1i} = \sqrt{2}Min[a, b]}$	$d_{2i} = 1\lambda$	$d_{3i} = 3\lambda$

Table 3.2 Preferred Spacing of Apertures in Orthogonal Orientation		
$\boldsymbol{d_{1x} = \frac{a+b}{2}}$	$d_{2x} = 1\lambda$	$d_{3x} = 2.8\lambda$
$\boldsymbol{d_{1y} = \frac{a+b}{2}}$	$d_{2y} = 1\lambda$	$d_{3y} = 2.8\lambda$
$\boldsymbol{d_{1i} = \sqrt{2}(\frac{Min[a, b]}{2} + \frac{a+b}{2})}$	$d_{2i} = 1\lambda$	$d_{3i} = 3\lambda$

5 Case Analysis: Simulation and Measurement

The methods discussed in Chapter 3 and 4 will be applied with the scattering formalism of mutual coupling (Chapter 2) for radiating rectangular apertures in this chapter. Then an error test was implemented for the computational algorithm by contrasting simulated results with measured one.

5.1 Examined Rectangular Non-uniform aperture Array Antenna

We used a polarization-agile antenna designed by Simeoni as the tested object in our thesis. The concept of this type of antennas was from [47], where a shared aperture antenna consisting of interleaved subarray with orthogonal, linear polarization was implemented. The advantage of this structure mainly results from the reduction of the feed network complexity and a narrow radiation beam. The properties are achieved through a trade-off with the antenna gain, which is roughly half of the gain of a uniform antenna with the same number of elements.

The tested antenna is composed by two interleaved subarrays with respectively 32 and 31 identical elements (shown on Fig. 5.1). In order to excite the vertical ('V') and horizontal ('H') Electric field, the elements in one subarray are placed with 90° rotation corresponding to the elements of the other subarray. This study is confined to the antenna front-end, each element being individually accessible via SMA connectors [48]. The elements are cavity-backed, stacked patches antennas fed by embedded pin-fed patches (see Fig. 5.2), which achieve the properties of wide operational bandwidth (200 MHz) and good isolation between channels. 16 through-vias are metal-plated surrounding the single structure, and whole array is fabricated in PCB technology by multilayer sandwich of RO4350B [49].

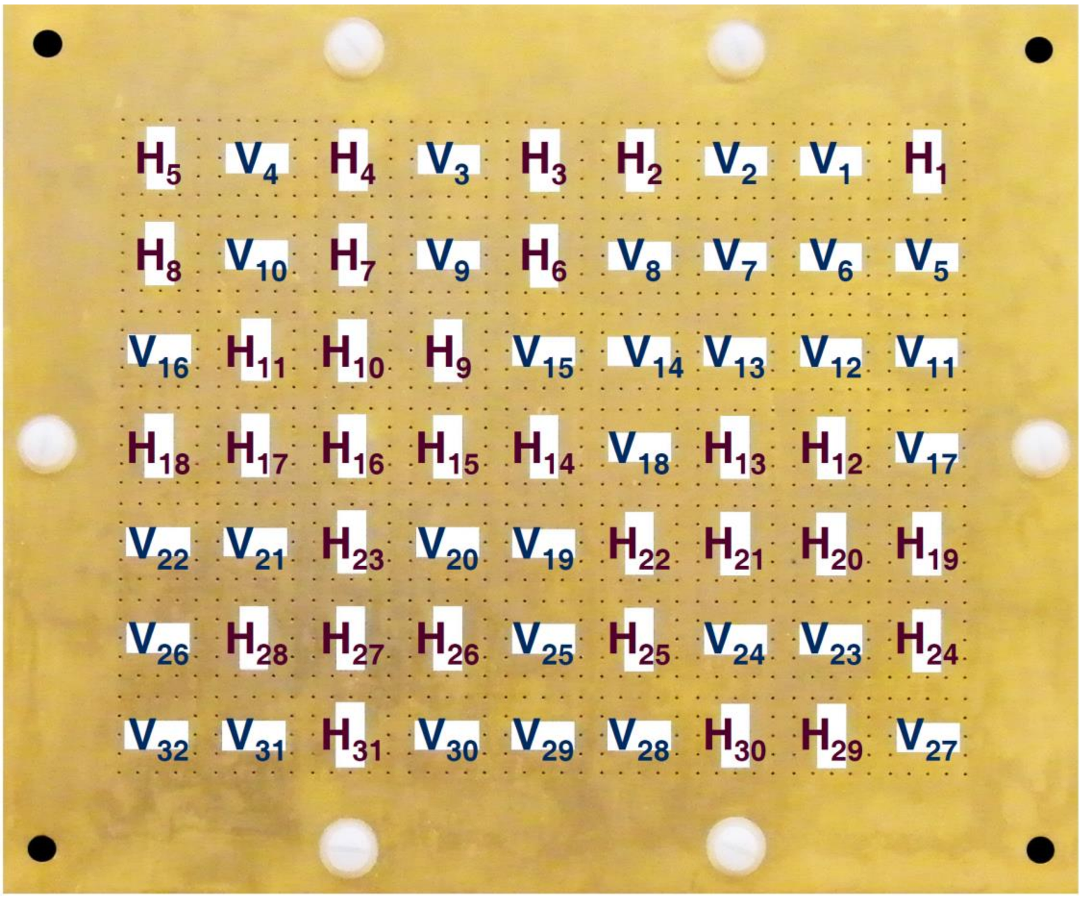

Figure 5.1 The polarization-agile antenna – front view, with the element counting, per subarray. The lattice is uniform with the identical steps $\Delta = 15\ mm$

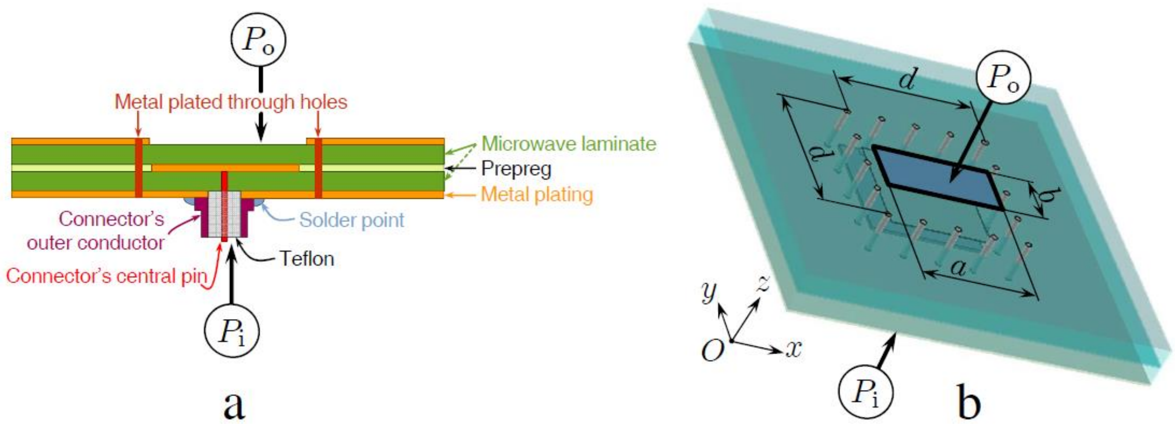

Figure 5.2 The element of polarization-agile antenna. (a) cross-section showing the internal stratification; (b) Scale illustration of the radiator. Main dimensions: $a = 9.7mm$, $b = 4.3mm$ and $d = 11.7mm$; the through-vias are spaced at $v_s = 2.925$mm; the embedded patch has the dimensions $p_x = 8.4mm$ and $p_y = 8.4mm$, is symmetrically placed with respect to the $x = 0$ plane and it is off-center by $s_y = 1.6mm$. Pi and Po denote the feeding coaxial port (input) and the rectangular aperture, radiating port (output), respectively.

5.2 Feasibility Analysis of Massimiliano's Design

In some cases we have analysed in Chapter 3 and 4, the error between the simulation and the reference was large. To make sure of the feasibility of our method in terms of Massimiliano's design, several tests were implemented in this section.

There are two types of coupling pairs in the antenna: 'V-V' ('H-H') and 'V-H' ('H-V'). As all elements are identical, the Bird's method can be used to estimate the coupling effect with low level error, which has been proved in Chapter 3.4.2. Unfortunately, the direct evaluation of couplings by Bird will become quickly computationally prohibitive with the increasing number of coupled apertures, thus other techniques are needed to solve the array. 2-D Interpolation was supposed to be applied to do a fast calculation of coupling admittance, but the approximation error can be relatively large with some specific aperture spacing shown in Chapter 4.2.

Here we made two tests on both 'V-V' and 'V-H' coupling pairs via 2-D Interpolation algorithm from Bailey, and the results are shown on Fig. 5.3 and Fig. 5.4 respectively. We did the error analysis both for the real value and imaginary value of the data, given as (5.1) and (5.2). Among all the plots in Fig. 5.3 and Fig. 5.4, there is a rectangle with black frame on behalf of the V type reference aperture. In order to filter out the overlapped or impractical cases (aperture boundary is placed within 2 mm), we disabled the related data where it shows up as a white rectangle in each plot.

$$Error^{R}_{Y,TE_{10}} = \left|\frac{Real(Y_{TE_{10},I}) - Real(Y_{TE_{10},MMM})}{\left|Y_{TE_{10},MMM}\right|_{max}}\right| \tag{5.1}$$

$$Error^{I}_{Y,TE_{10}} = \left|\frac{Imag(Y_{TE_{10},I}) - Imag(Y_{TE_{10},MMM})}{\left|Y_{TE_{10},MMM}\right|_{max}}\right| \tag{5.2}$$

where $Y_{TE_{10},I}$ is the interpolated admittance and $Y_{TE_{10},MMM}$ represents the result from the Bird's mode matching method.

By looking at the values in the plots, we found the error for the 'V-V' case is acceptable, where the maximum errors of real and imaginary value are 6% and 3.3% respectively. If people consider the 15 mm spacing between nearby element centres in the physical layout, the error could be even lower at nearly zero. On the contrary, the 'V-H' case has relatively higher error compared with 'V-V' ones. Although 14% error for real part and 33% error for imaginary part are beyond the tolerance, they are both in an extreme low level on the $45°$ diagonal direction. In the physical configuration, all the nearby 'V-H' coupling pairs are placed in $45°$ diagonal direction with $15\sqrt{2}\ mm$. Thus 2-D Interpolation will also achieve a good approximation for 'V-H' coupling in this polarization-agile antenna.

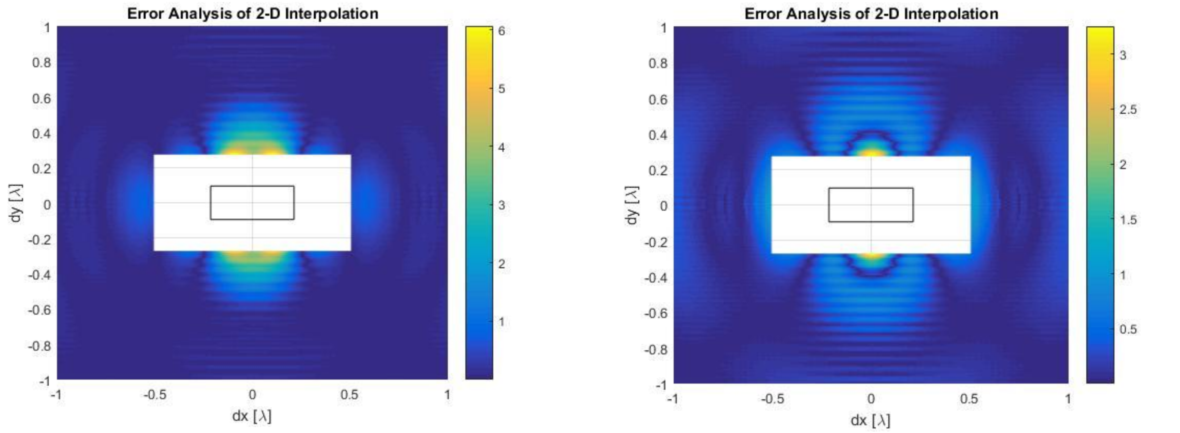

(a) (b)

Figure 5.3 Error Plot of 2-D Interpolation for case V-V. (a) Real Part Error; (b) Imaginary Part Error

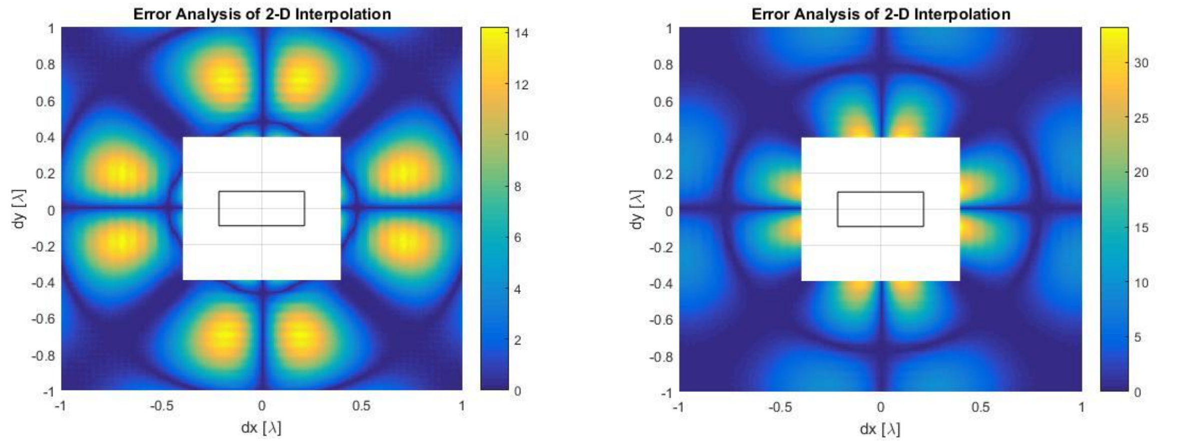

(a) (b)

Figure 5.4 Error Plot of 2-D Interpolation for case V-H. (a) Real Part Error; (b) Imaginary Part Error

5.3 Simulation and Measurement

The reflection coefficients of all 63 elements on the tested array were measured by a setup of an Agilent Technologies E8364B vector network analyser and an Agilent Technologies 87050-K24 – full 2×24 crossbar mechanical switch test-set. A 2 m cable for calibration was used to connect the switch test-set to every single radiator, while other ports were closed on matching loads in the meantime. The whole structure was placed in an isolated observing room with absorbers pasted on inner wall to minimizing unexpected reflection. The measurement results are shown on Fig. 5.5. The variations are obvious with the physical layout of the antenna – different levels of feed matching and slight variations in resonant frequencies. The best matching apertures were observed as H_{20}, H_{21} and H_{27} (H-subarray), and V_7, V_{14}, V_{25} as well as V_{26} (V-subarray), where all the mentioned elements have a quasi-uniform neighbourhood. The resonant frequencies vary between 13.11GHz and 13.25GHz, with a mean of $f_{r,m} = 13.19GHz$ and a standard deviation $\sigma = 28.4MHz$.

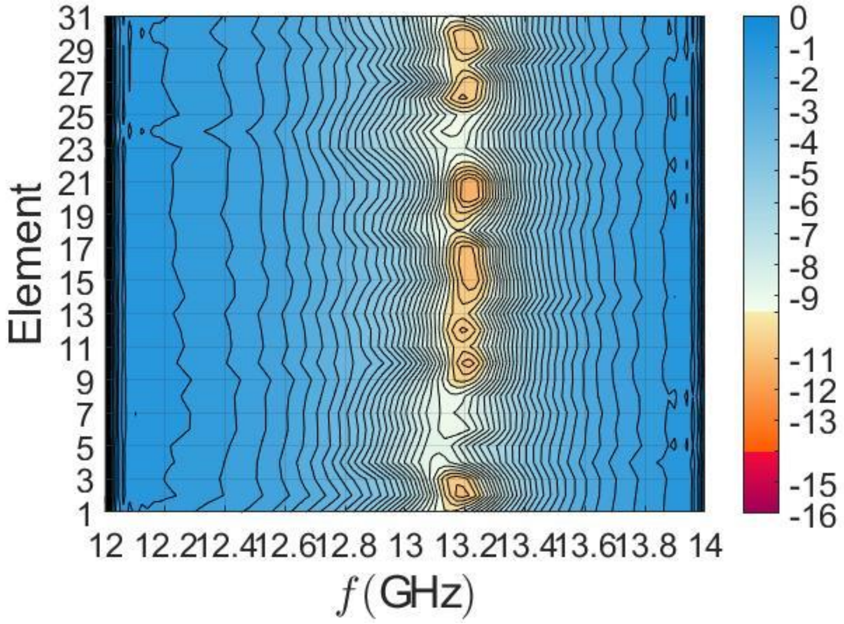

(a)

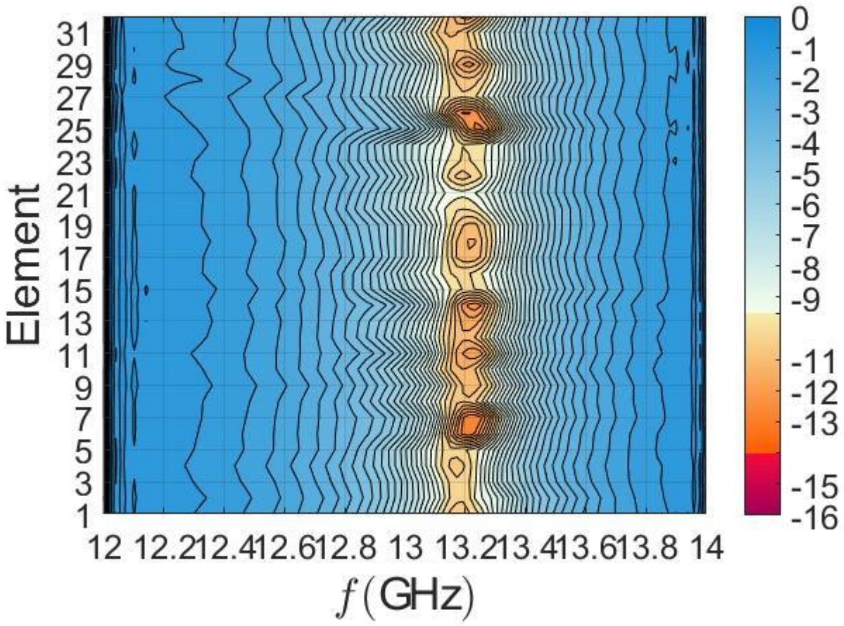

(b)

Figure 5.5 Measured Reflection Coefficients for Subarrays of the Polarization-agile Antenna. (a) “H” type subarray; (b) “V” type subarray.

The computational strategy introduced in Chapter 2 was implemented in Matlab. On the one hand, the couplings S_{el} between the TEM mode at P_i and the aperture modes at P_o (see Fig. 5.2) were evaluated by CST simulation. On the other hand, the processes, including Assembling GAM_{rad} via interpolation, obtaining S_{rad} by conversion and overall computation (combining S_{el} and S_{rad} into S_{active}), were coded in Matlab. The featured times of the computation are provided in Table 5.1, for which a workstation with a $3.1\ GHz$ processor and a $32\ GB$ RAM was used. Please note that it achieved a $2200-fold$ running time reduction by employing interpolation to assemble GAM_{rad}, instead of Bird’s mode matching method.

We have tried using the pure computational approach, which took nearly 2 hours accounting for only 2 apertures. Undoubtedly, it is of nonsense to apply the method for this real case where it will cost 3906 hours in principle for GAM_{rad} with 63 apertures. Nonetheless, a corresponding processing structure is developed in terms of the simulation strategy (see Fig. 5.6. Within the structure, step 1 and 2 only need to be calculated once and saved for any given element combination. Effective steps from 3 to 5 will be processed every optimization scheme with the change of element placement.

TABLE 5.1

FEATURE COMPUTATION TIMES FOR 100 FREQUENCY SAMPLES.

	Algorithm's Block	Computation Time
1	Reference Aperture modal Coupling Evaluation 4 coupling types × 9 apertures × 10 modes	29.5 mins
2	Calculation of S_{el} via CST Simulation	6.5 mins
3	Assembling GAM_{rad} via Interpolation 63 apertures × 10 modes	5.7 seconds
4	Converting GAM_{rad} into S_{rad}	19.1 seconds
5	Combining S_{el} and S_{rad} into S_{active}	110 seconds
	Assembling GAM_{rad} by Bird's MMM 63 apertures × 10 modes	**35.5 hours**

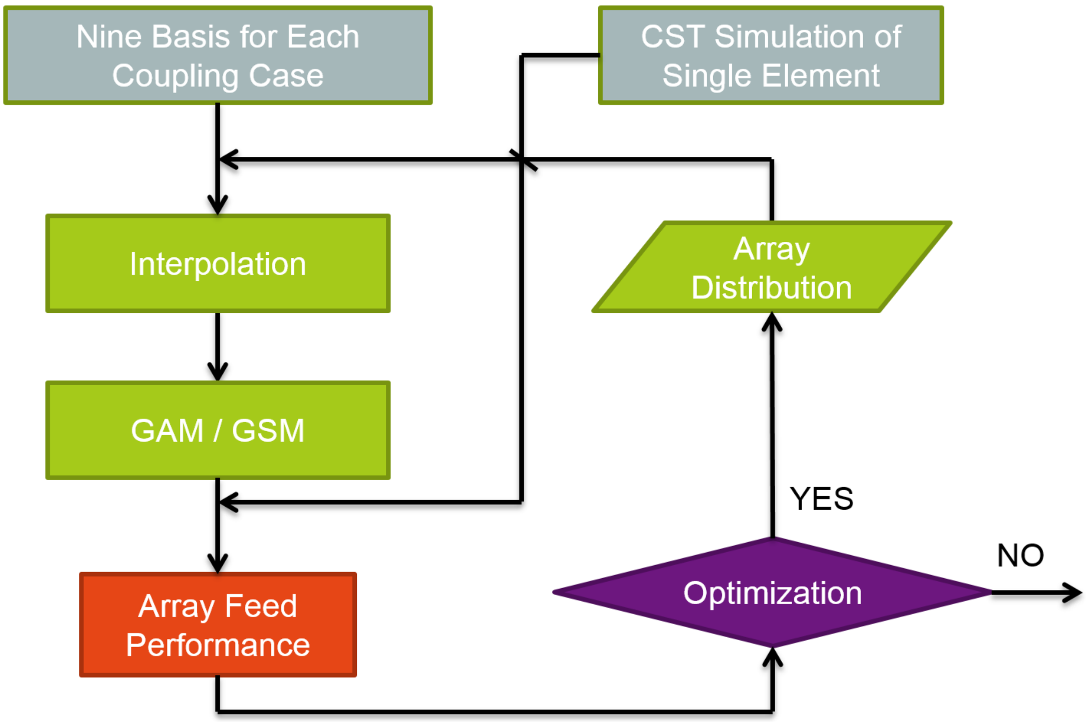

Figure 5.6 Flow Chart of Processing Structure

The simulated reflection coefficients at feed port of each aperture were obtained via the steps shown on Fig. 5.6, and the accuracy of the proposed analytical method was validated by comparing the data with the measured one in Fig. 5.3. Here is the simulated results (Fig. 5.7). A slight adjust on relative permittivity was made in order to match the measurement result.

Because the reference value of the relative permittivity of the real material in guidebook is an average number, where the real one may vary within certain range in fabrication [47].

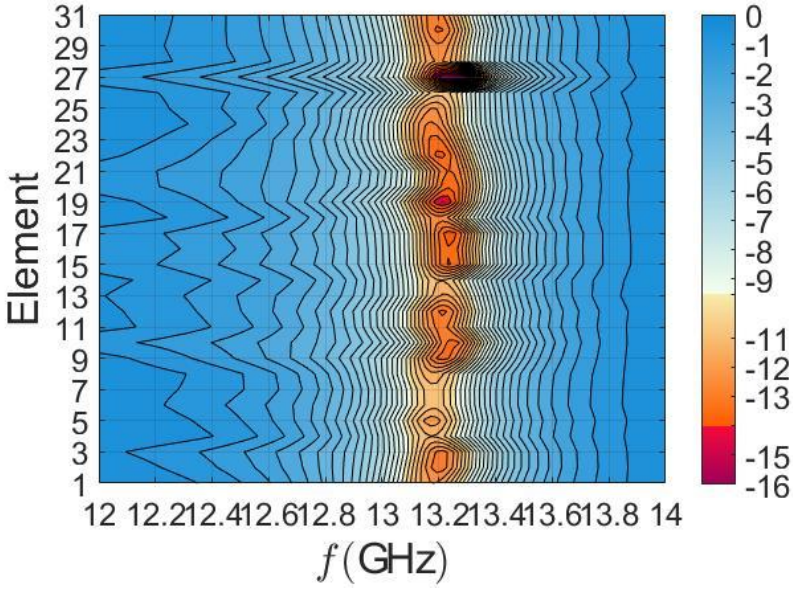

(a)

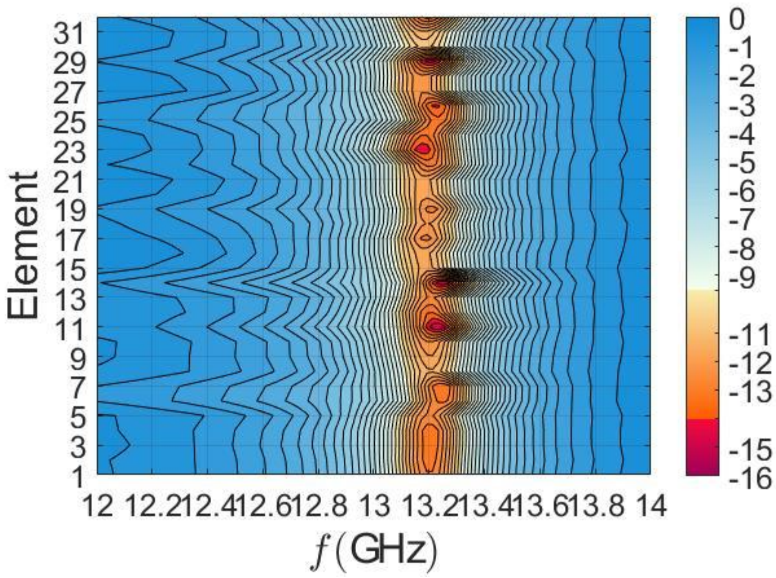

(b)

Figure 5.7 Simulated Reflection Coefficients for Subarrays of the Polarization-agile Antenna. (a) "H" type subarray; (b) "V" type subarray.

Matching level patterns and resonant frequency fluctuations of the simulation are illustrated, and a rough similarity upon measurement results can be observed. However, the simulated resonance $|S_{11}|$ levels are about $3 - 4\ dB$ below the measured ones. To better illustrate this, the smallest and largest differences are shown in Fig. 5.8.(a). This discrepancy is attributed to: (i) the additional reflections caused by the actual SMA connectors and mounting imperfections that were not included in the CST model; (ii) the simulations assume an infinitely extended flange and cannot account for reflections caused by the edges of a finite flange and (iii) the measurement results were also affected by small, but non-negligible reflections from the enclosure's walls. Apart from the matching level, a quantitative comparison of resonant frequency between simulated $f_r^S(i)$ and measured $f_r^M(i)$ is made. The relative deviation $\Delta_{f_r}(i)$ is shown in Fig. 5.8.(b). The maximum deviation is less than 0.5% which is a convincing proof of the simulation's accuracy.

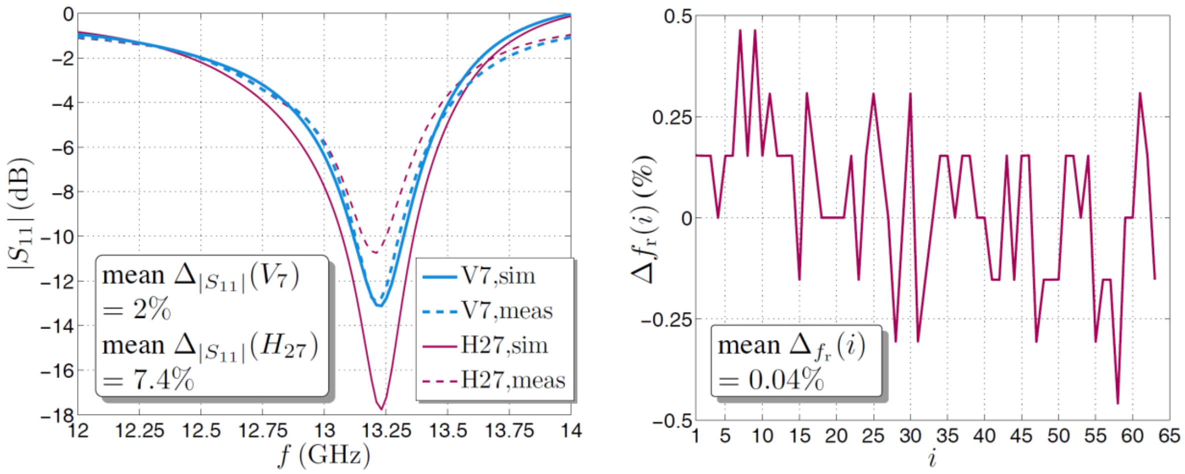

Figure 5.8 Deviations between measured and simulated results. (a) Comparison of $|S_{11}^M|$ and $|S_{11}^S|$ for the elements with the best (V_7) and worst (H_{27}) approximations; (b) resonant frequency deviations. $\Delta[S_{11}(i)] = \left|S_{11,dB}^M(i) - S_{11,dB}^S(i)\right| / max\left(S_{11,dB}^S(i')\right)$, mean calculated over the frequency band.

6 Conclusion

6.1 Summary

In this thesis, a complete tool for evaluating the mutual coupling in non-uniform (interleaved) array antennas of rectangular aperture radiators was presented. The results were obtained by assembling scattering matrix of interaction and each single element. Bird's MMM and Bailey's interpolation method were used to evaluate the air interaction scattering matrix, while the single element behavior needed to be simulated by software, such as CST. Several steps were adopted in order to increase the efficiency and quality of our strategy, for instance deriving fast algorithm of Bird's MMM, seeking for best spacing for 2D-Interpolation and error test for each process.

The processing structure was optimized in terms of efficiency for the strategy. The methods computational efficiency and accuracy were convincingly demonstrated by analyzing an interleaved array antenna consisting of 31+32 cavity-backed apertures for which full measurement results were available:

1. The full evaluation of all coupling admittances corresponding to 10 modes/aperture required only 5.7 seconds, a factor 2200 down from the computation time required for calculating these couplings with an already streamlined direct integration scheme.

2. The calculated resonance frequencies at all 63 feeding ports deviated by less than 0.5% from the measured values.

These features clearly indicate that our computational engine is exceptionally well-placed for being included in array optimization strategy. This conclusion is also supported by the fact that a paper describing its philosophy and the comparisons with the above mentioned interleaved array was just accepted for publication in IEEE Antennas and Wireless Propagation Letters, with a second paper being submitted to the European Conference on Antennas and Propagation EuCAP 2018.

6.2 Limitation of the Strategy

The tool, in our point of view, can achieve an efficient and light simulation for any non-uniform array antennas of rectangular apertures with arbitrary element placement. However, there are limitations and uncertainty. In some special cases (for example, calculating coupling between evanescent mode and active mode between two different apertures), the coupling admittance from Bird's MMM does not match well with the result of CST simulation, and CST are also not reliable beyond that situation. Moreover, 2D-Interpolation may suffer large relative error for specific coupling apertures, which has been discussed in Chapter 4.2.3.

6.3 Future Work

By finishing this research, several aspects that would require further investigation have been identified:

1) A reliable tool for evaluating the coupling effect between evanescent mode and active mode between different apertures needs to be found as reference. Figuring out how CST think about the problem could be a preferable choice of this issue.

2) Due to the poor performance 2D-Interpolation did in some circumstances, an adapted method is required. Instead of taking reference apertures along x-axis, y-axis and $45°$ diagonal, we would like to rearrange the positions of the reference apertures. We believe the method will then acquire higher flexibility, thus better feasibility dealing with specific cases is achieved.

3) The strategy for far-field pattern simulation needs to be developed. By cascading the scattering matrix between elements and free space, wave-field expansion can be calculated via certain intermedia values referred to (3.1) and (3.2). Then the far-field pattern is available via superposition of the far-field of each element. A measurement for radiation pattern will be also important as the reference of this far-field pattern strategy.

7 Appendix

A. Field Expression of Rectangular Waveguide based on Maxwell's Equations

For the electromagnetic field within the waveguide with a lossless material, we have the Maxwell's Equations as:

$$\nabla \times \boldsymbol{H} = j\omega\epsilon\boldsymbol{E} \tag{A.1}$$
$$\nabla \times \boldsymbol{E} = -j\omega\mu\boldsymbol{H} \tag{A.2}$$
$$\nabla \cdot \boldsymbol{H} = \frac{\rho_v}{\mu} \tag{A.3}$$
$$\nabla \cdot \boldsymbol{E} = 0 \tag{A.4}$$

In this step, the Eqn (A.1) and (A.2) were rewritten in terms of longitude component and transverse components in Table A1 [50, Chapter 17.2].

Table A1 Maxwell's curl equations and their transverse components

Electric field expressions		Magnetic field expressions	
$\frac{\partial H_z}{\partial y} - \frac{\partial H_y}{\partial z} = j\omega\epsilon E_x$	(A.5)	$\frac{\partial E_z}{\partial y} - \frac{\partial E_y}{\partial z} = -j\omega\mu H_x$	(A.8)
$\frac{\partial H_x}{\partial z} - \frac{\partial H_z}{\partial x} = j\omega\epsilon E_y$	(A.6)	$\frac{\partial E_x}{\partial z} - \frac{\partial E_z}{\partial x} = -j\omega\mu H_y$	(A.9)
$\frac{\partial H_y}{\partial x} - \frac{\partial H_x}{\partial y} = j\omega\epsilon E_z$	(A.7)	$\frac{\partial E_y}{\partial x} - \frac{\partial E_x}{\partial y} = -j\omega\mu H_z$	(A.10)

Then a plane wave assumption along $+z$ direction with propagation constant γ was applied for the field model. Then we acquire a group of new derivative forms respected to z direction:

$$\frac{\partial H_y}{\partial z} = -\gamma H_y, \quad \frac{\partial H_x}{\partial z} = -\gamma H_x, \quad \frac{\partial E_y}{\partial z} = -\gamma E_y, \quad \frac{\partial E_x}{\partial z} = -\gamma E_x \tag{A.11}$$

Now, the Eqn (A.5) - (A.10) were transformed into (A.12) – (A.17):

$\frac{\partial H_z}{\partial y} + \gamma H_y = j\omega\epsilon E_x$	(A.12)	$\frac{\partial E_z}{\partial y} + \gamma E_y = -j\omega\mu H_x$	(A.15)
$-\gamma H_x - \frac{\partial H_z}{\partial x} = j\omega\epsilon E_y$	(A.13)	$-\gamma E_x - \frac{\partial E_z}{\partial x} = -j\omega\mu H_y$	(A.16)
$\frac{\partial H_y}{\partial x} - \frac{\partial H_x}{\partial y} = j\omega\epsilon E_z$	(A.14)	$\frac{\partial E_y}{\partial x} - \frac{\partial E_x}{\partial y} = -j\omega\mu H_z$	(A.17)

By substituting H_y from (3-16) into (3-12), we can obtain the electric field expression in x direction:

$$\frac{\partial H_z}{\partial y} + \frac{\gamma\left(\gamma E_x - \frac{\partial E_z}{\partial x}\right)}{j\omega\mu} = j\omega\epsilon E_x \tag{A.18}$$

With transformation applying $k = \omega\sqrt{\epsilon\mu}$ and $k_c = \sqrt{\gamma^2 + k^2}$ (cut-off frequency) we have

$$E_x = \frac{1}{k_c^2}\left(-\gamma\frac{\partial E_z}{\partial x} - j\omega\mu\frac{\partial H_z}{\partial y}\right) \tag{A.19}$$

Similarly, we obtain the other three transverse components as

$$E_y = \frac{1}{k_c^2}\left(-\gamma \frac{\partial E_z}{\partial y} + j\omega\mu \frac{\partial H_z}{\partial x}\right) \tag{A.20}$$

$$H_x = \frac{1}{k_c^2}\left(-\gamma \frac{\partial H_z}{\partial x} + j\omega\epsilon \frac{\partial E_z}{\partial y}\right) \tag{A.21}$$

$$H_y = \frac{1}{k_c^2}\left(-\gamma \frac{\partial H_z}{\partial y} - j\omega\epsilon \frac{\partial E_z}{\partial x}\right) \tag{A.22}$$

In the case of transverse electric (TE) field, $E_z = 0$ where the only field component in the propagation direction is H_z. Substituting $E_z = 0$ into the Eqn (3-19) to (3-22), simplified forms were acquired as:

$$E_x = \frac{-j\omega\mu}{k_c^2}\left(\frac{\partial H_z}{\partial y}\right) \tag{A.23}$$

$$E_y = \frac{j\omega\mu}{k_c^2}\left(\frac{\partial H_z}{\partial x}\right) \tag{A.24}$$

$$H_x = \frac{-\gamma}{k_c^2}\left(\frac{\partial H_z}{\partial x}\right) \tag{A.25}$$

$$H_y = \frac{-\gamma}{k_c^2}\left(\frac{\partial H_z}{\partial y}\right) \tag{A.26}$$

By taking the derivative of (3-23) and (3-24) to reform the (3-10), we obtained (3-27), which can be also seen as a Helmholtz equation.

$$\frac{\partial^2 H_z}{\partial x^2} + \frac{\partial^2 H_z}{\partial y^2} + k_c^2 H_z = 0, \qquad for\ TE\ waves \tag{A.27}$$

Repeating the similar steps with assumption of transverse magnetic (TM) wave, we found another Helmholtz Eqn (3-28). Any field problem of waveguide in different propagation mode can be solve by using (3-27) and (3-28) with proper boundary conditions.

$$\frac{\partial^2 E_z}{\partial x^2} + \frac{\partial^2 E_z}{\partial y^2} + k_c^2 E_z = 0, \qquad for\ TM\ waves \tag{A.28}$$

To solve the Helmholtz Eqn (3-27) and (3-28) with boundary conditions of the rectangular waveguides in whether TE or TM mode, the field expressions were acquired in Table A2. In order to give the solution, assumptions from [50, Chapter 5.4.4.1] were applied.

Table A2 Solution of Helmholtz equation and their transverse components		
	TE wave field expressions	TM wave field expressions
E_x	$\frac{j\omega\mu}{k_c^2} H_0 \frac{n\pi}{b} \cos\left(\frac{m\pi}{a}x\right)\ \sin\left(\frac{n\pi}{b}y\right) e^{-\gamma z}$	$-\frac{\gamma}{k_c^2} E_0 \frac{m\pi}{a} \cos\left(\frac{m\pi}{a}x\right)\ \sin\left(\frac{n\pi}{b}y\right) e^{-\gamma z}$
E_y	$-\frac{j\omega\mu}{k_c^2} H_0 \frac{m\pi}{a} \sin\left(\frac{m\pi}{a}x\right)\ \cos\left(\frac{n\pi}{b}y\right) e^{-\gamma z}$	$-\frac{\gamma}{k_c^2} E_0 \frac{n\pi}{b} \sin\left(\frac{m\pi}{a}x\right)\ \cos\left(\frac{n\pi}{b}y\right) e^{-\gamma z}$
E_z	0	$E_0 \sin\left(\frac{m\pi}{a}x\right)\ \sin\left(\frac{n\pi}{b}y\right) e^{-\gamma z}$
H_x	$\frac{\gamma}{k_c^2} H_0 \frac{m\pi}{a} \sin\left(\frac{m\pi}{a}x\right)\ \cos\left(\frac{n\pi}{b}y\right) e^{-\gamma z}$	$\frac{j\omega\epsilon}{k_c^2} E_0 \frac{n\pi}{b} \sin\left(\frac{m\pi}{a}x\right)\ \cos\left(\frac{n\pi}{b}y\right) e^{-\gamma z}$
H_y	$\frac{\gamma}{k_c^2} H_0 \frac{n\pi}{b} \cos\left(\frac{m\pi}{a}x\right)\ \sin\left(\frac{n\pi}{b}y\right) e^{-\gamma z}$	$-\frac{j\omega\epsilon}{k_c^2} E_0 \frac{m\pi}{a} \cos\left(\frac{m\pi}{a}x\right)\ \sin\left(\frac{n\pi}{b}y\right) e^{-\gamma z}$
H_z	$H_0 \cos\left(\frac{m\pi}{a}x\right)\ \cos\left(\frac{n\pi}{b}y\right) e^{-\gamma z}$	0

B. Fast Algorithm of Bird's Method

This is the most general admittance expression for rectangular waveguide and can be found directly in Bird's paper, which is

$$y_{i,j}(m,n|m',n') = \frac{jkY_0}{4\pi}\alpha_{mn}\alpha_{m'n'}\left(c_x I_x + c_y I_y - c_z I_z\right) \quad \text{(B.1)}$$

Where

$$\begin{matrix} I_x \\ I_y \\ I_z \end{matrix} = \iint_{D_i} dS \iint_{D_j} dS' \, G(x-x', y-y')$$
$$* \begin{matrix} sin \\ cos \\ cos \end{matrix}\left(\frac{m\pi x}{a_i}\right) \begin{matrix} cos \\ sin \\ cos \end{matrix}\left(\frac{n\pi y}{b_i}\right) \begin{matrix} sin \\ cos \\ cos \end{matrix}\left(\frac{m'\pi(x'-\Delta x)}{a_j}\right) \begin{matrix} cos \\ sin \\ cos \end{matrix}\left(\frac{n'\pi(y'-\Delta y)}{b_j}\right) \quad \text{(B.2)}$$

$$\alpha_{mn} = \sqrt{\frac{2\epsilon_{0m}\epsilon_{0n}}{a_i b_i Y_{mn} k_{c,mn}^2}}$$

And $c_x, c_y, c_z, \epsilon_{0m}, \epsilon_{0n}$ are some fixed variables for the equation

Then we assume

$$I_{sin}^1(x,x',y,y',m,m',a_i,a_j,\Delta x) = \int_0^{a_i} dx \int_{\Delta x}^{\Delta x + a_j} dx' \, G(x-x', y-y')\sin(\frac{m\pi x}{a_i})\sin(\frac{m'\pi(x'-\Delta x)}{a_j}) \quad \text{(B.3.1)}$$

$$I_{cos}^1(x,x',y,y',m,m',a_i,a_j,\Delta x) = \int_0^{a_i} dx \int_{\Delta x}^{\Delta x + a_j} dx' \, G(x-x', y-y')\cos(\frac{m\pi x}{a_i})\cos(\frac{m'\pi(x'-\Delta x)}{a_j}) \quad \text{(B.3.2)}$$

$$I_{sin}^2(y,y',n,n',b_i,b_j,\Delta y) = \int_0^{b_i} dy \int_{\Delta y}^{\Delta y + b_j} dy' \sin(\frac{n\pi y}{b_i})\sin(\frac{n'\pi(y'-\Delta y)}{b_j}) \quad \text{(B.3.3)}$$

$$I_{cos}^2(y,y',n,n',b_i,b_j,\Delta y) = \int_0^{b_i} dy \int_{\Delta y}^{\Delta y + b_j} dy' \cos(\frac{n\pi y}{b_i})\cos(\frac{n'\pi(y'-\Delta y)}{b_j}) \quad \text{(B.3.4)}$$

Therefore the Eqn (B.2) can be rewritten as

$$\begin{matrix} I_x \\ I_y \\ I_z \end{matrix} = \begin{matrix} I_{sin}^1 \cdot I_{cos}^2 \\ I_{cos}^1 \cdot I_{sin}^2 \\ I_{cos}^1 \cdot I_{cos}^2 \end{matrix} \quad \text{(B.4)}$$

where $\Delta x = x_0' - x_0$ *and* $\Delta y = y_0' - y_0$, which is the edge point distance of two rectangular waveguide. We show it in Figure 1 where $x_0 = 0, y_0 = 0$.

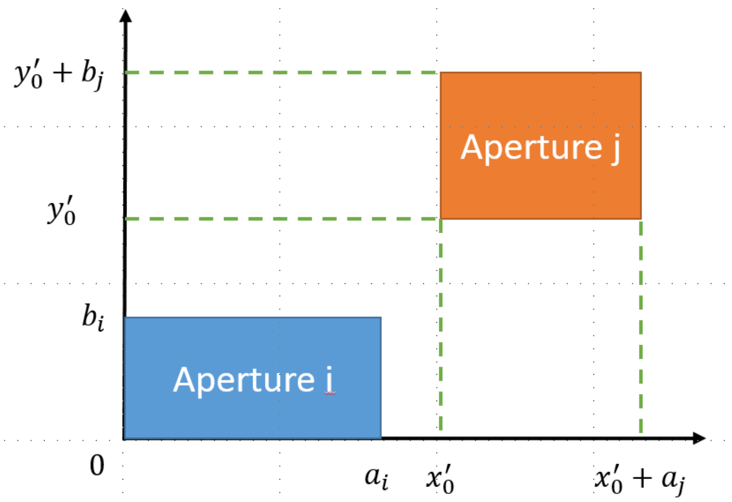

Figure 1 Illustration of Positions for Two Aperture

Let's first consider the Eqn (B.3.2). The integral domain for that case is shown in Figure 2. At this stage, four new variables are defined for the solution of the equation, namely $\sigma = x - x' + \Delta_x, v = x + x' - a_i - \Delta_x, \lambda = y - y' + \Delta_y$ and $u = y + y' - b_i - \Delta_y$, then the integral domain become the one depicted on Figure 3. And the Eqn (B.3.2) is transferred to (B.5).

$$\begin{aligned} & I_{cos}^{1}(\sigma, v, \lambda, m, m', a_i, a_j, \Delta_x, \Delta_y) \\ & = \frac{1}{2}\int_{-a_j}^{a_i} d\sigma \int_{-a_i+\sigma}^{2a_j-a_i+\sigma} dv\, G(\sigma - \Delta_x, \lambda - \Delta_y) T_{cos}(\sigma, v, \lambda, m, m', a_i, a_j, \Delta_x) \\ & - \frac{1}{2}\int_{-a_j}^{0} d\sigma \int_{-a_i+\sigma}^{-a_i-\sigma} dv\, G(\sigma - \Delta_x, \lambda - \Delta_y) T_{cos}(\sigma, v, \lambda, m, m', a_i, a_j, \Delta_x) \\ & - \frac{1}{2}\int_{a_i-a_j}^{a_i} d\sigma \int_{a_i-\sigma}^{2a_j-a_i+\sigma} dv\, G(\sigma - \Delta_x, \lambda - \Delta_y) T_{cos}(\sigma, v, \lambda, m, m', a_i, a_j, \Delta_x) \\ & \qquad = I_A - I_B - I_C \end{aligned} \tag{B.5}$$

where

$$\begin{aligned} & T_{cos}(\sigma, v, \lambda, m, m', a_i, a_j, \Delta_x) \\ & \qquad = \cos(\frac{m\pi(v + a_i + \Delta_x + \sigma)}{2a_i})\cos(\frac{m'\pi(v + a_i + \Delta_x - \sigma)}{2a_j}) \end{aligned} \tag{B.6}$$

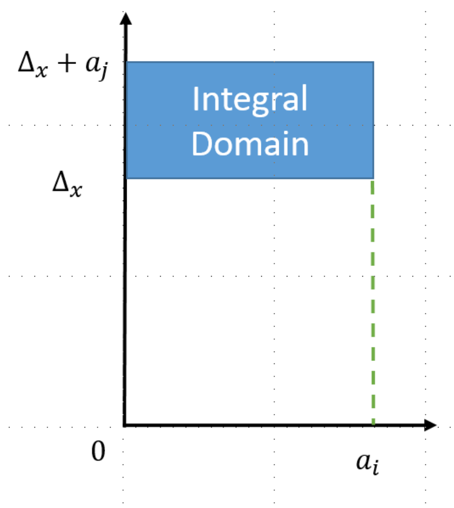

Figure 2 Illustration of Integral domain for Equation (B.3.2)

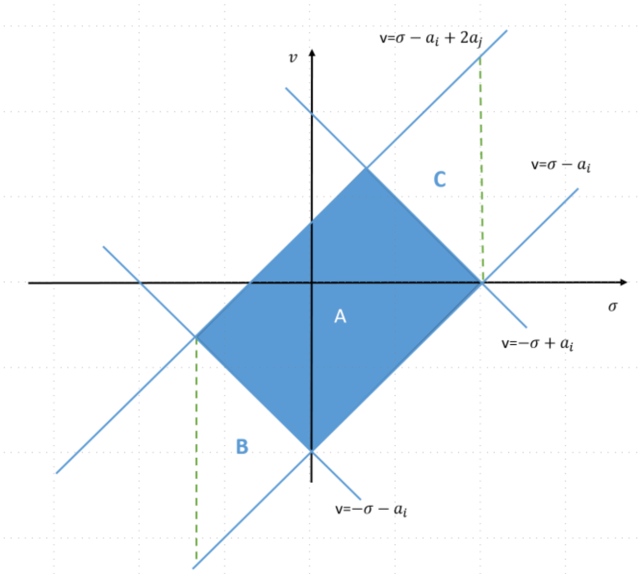

Figure 3 Illustration of Changed Integral domain for Equation (B.3.2)

By some mathematical steps, we can changed the (B.3.2) into a new form which is easier to do the integral separately.

$$
\begin{aligned}
T_{cos}(\sigma, v, a_i, a_j, dx) &= \left[cos\frac{m\pi(v+ai)}{2a_i}\cos\left(\frac{m\pi\sigma}{2a_i}\right) - sin\frac{m\pi(v+ai)}{2a_i}\sin\left(\frac{m\pi\sigma}{2a_i}\right)\right] \\
&* \left[cos\frac{m'\pi(v+ai)}{2a_j}\cos\left(\frac{m'\pi\sigma}{2a_j}\right) + sin\frac{m'\pi(v+ai)}{2a_j}\sin\left(\frac{m'\pi\sigma}{2a_j}\right)\right] \\
&= \cos\left(\frac{m\pi\sigma}{2a_i}\right)\cos\left(\frac{m'\pi\sigma}{2a_j}\right) cos\frac{m\pi(v+ai)}{2a_i} cos\frac{m'\pi(v+ai)}{2a_j} \\
&+ \cos\left(\frac{m\pi\sigma}{2a_i}\right)\sin\left(\frac{m'\pi\sigma}{2a_j}\right) cos\frac{m\pi(v+ai)}{2a_i} sin\frac{m'\pi(v+ai)}{2a_j} \\
&- \sin\left(\frac{m\pi\sigma}{2a_i}\right)\cos\left(\frac{m'\pi\sigma}{2a_j}\right) sin\frac{m\pi(v+ai)}{2a_i} cos\frac{m'\pi(v+ai)}{2a_j} \\
&- \sin\left(\frac{m\pi\sigma}{2a_i}\right)\sin\left(\frac{m'\pi\sigma}{2a_j}\right) sin\frac{m\pi(v+ai)}{2a_i} sin\frac{m'\pi(v+ai)}{2a_j} \\
&= T_A^1(\sigma, v, m, m', a_i, a_j) + T_A^2(\sigma, v, m, m', a_i, a_j) \\
&+ T_A^3(\sigma, v, m, m', a_i, a_j) + T_A^4(\sigma, v, m, m', a_i, a_j) \qquad \text{(B.7)}
\end{aligned}
$$

A combination of Eqn (B.5) and Eqn (B.7) can be made as

$$
\begin{aligned}
I_A = \frac{1}{2}\int_{-a_j}^{a_i} d\sigma \int_{-a_i+\sigma}^{2a_j-a_i+\sigma} dv\, G(\sigma - \Delta_x, \lambda - \Delta_y) \\
* \left[T_A^1(\sigma, v, m, m', a_i, a_j) + T_A^2(\sigma, v, m, m', a_i, a_j)\right. \\
\left. + T_A^3(\sigma, v, m, m', a_i, a_j) + T_A^4(\sigma, v, m, m', a_i, a_j)\right] \\
= I_A^1 + I_A^2 + I_A^3 + I_A^4 \qquad \text{(B.8)}
\end{aligned}
$$

where

$$I_A^1 = \frac{1}{2}\int_{-a_j}^{a_i} G(\sigma - \Delta_x, \lambda - \Delta_y)\cos\left(\frac{m\pi\sigma}{2a_i}\right)\cos\left(\frac{m'\pi\sigma}{2a_j}\right)d\sigma$$

$$* \int_{-a_i+\sigma}^{2a_j-a_i+\sigma} cos\,\frac{m\pi(v+a_i)}{2a_i}\,cos\,\frac{m'\pi(v+a_i)}{2a_j}dv$$

$$= \frac{1}{2}\int_{-a_j}^{a_i} G(\sigma - \Delta_x, \lambda - \Delta_y)\cos\left(\frac{m\pi\sigma}{2a_i}\right)\cos\left(\frac{m'\pi\sigma}{2a_j}\right)d\sigma$$

$$* \int_{-a_i+\sigma}^{2a_j-a_i+\sigma} \frac{1}{2}\left\{cos\left[\frac{\pi}{2}\left(\frac{m}{a_i}+\frac{m'}{a_j}\right)(v+a_i)\right] + cos\left[\frac{\pi}{2}\left(\frac{m}{a_i}-\frac{m'}{a_j}\right)(v+a_i)\right]\right\}dv$$

$$= \frac{1}{2}\int_{-a_j}^{a_i} G(\sigma - \Delta_x, \lambda - \Delta_y)\cos\left(\frac{m\pi\sigma}{2a_i}\right)\cos\left(\frac{m'\pi\sigma}{2a_j}\right)d\sigma * a_j$$

$$* \left\{cos\left[\frac{\pi}{2}\left(\frac{m}{a_i}+\frac{m'}{a_j}\right)(\sigma+a_j)\right] sinc\left[\frac{\pi}{2}\left(\frac{m}{a_i}+\frac{m'}{a_j}\right)a_j\right]\right.$$

$$\left. + cos\left[\frac{\pi}{2}\left(\frac{m}{a_i}-\frac{m'}{a_j}\right)(\sigma+a_j)\right] sinc\left[\frac{\pi}{2}\left(\frac{m}{a_i}-\frac{m'}{a_j}\right)a_j\right]\right\} \qquad \text{(B.8.1)}$$

By using the similar steps, we have

$$I_A^2 = \frac{1}{2}\int_{-a_j}^{a_i} G(\sigma - \Delta_x, \lambda - \Delta_y)\cos\left(\frac{m\pi\sigma}{2a_i}\right)\sin\left(\frac{m'\pi\sigma}{2a_j}\right)d\sigma * a_j$$

$$* \left\{sin\left[\frac{\pi}{2}\left(\frac{m}{a_i}+\frac{m'}{a_j}\right)(\sigma+a_j)\right] sinc\left[\frac{\pi}{2}\left(\frac{m}{a_i}+\frac{m'}{a_j}\right)a_j\right]\right.$$

$$\left. - sin\left[\frac{\pi}{2}\left(\frac{m}{a_i}-\frac{m'}{a_j}\right)(\sigma+a_j)\right] sinc\left[\frac{\pi}{2}\left(\frac{m}{a_i}-\frac{m'}{a_j}\right)a_j\right]\right\} \qquad \text{(B.8.2)}$$

$$I_A^3 = -\frac{1}{2}\int_{-a_j}^{a_i} G(\sigma - \Delta_x, \lambda - \Delta_y)\sin\left(\frac{m\pi\sigma}{2a_i}\right)\cos\left(\frac{m'\pi\sigma}{2a_j}\right)d\sigma * a_j$$

$$* \left\{sin\left[\frac{\pi}{2}\left(\frac{m}{a_i}+\frac{m'}{a_j}\right)(\sigma+a_j)\right] sinc\left[\frac{\pi}{2}\left(\frac{m}{a_i}+\frac{m'}{a_j}\right)a_j\right]\right.$$

$$\left. + sin\left[\frac{\pi}{2}\left(\frac{m}{a_i}-\frac{m'}{a_j}\right)(\sigma+a_j)\right] sinc\left[\frac{\pi}{2}\left(\frac{m}{a_i}-\frac{m'}{a_j}\right)a_j\right]\right\} \qquad \text{(B.8.3)}$$

$$I_A^4 = -\frac{1}{2}\int_{-a_j}^{a_i} G(\sigma - \Delta_x, \lambda - \Delta_y)\sin\left(\frac{m\pi\sigma}{2a_i}\right)\sin\left(\frac{m'\pi\sigma}{2a_j}\right)d\sigma * a_j$$

$$* \left\{-cos\left[\frac{\pi}{2}\left(\frac{m}{a_i}+\frac{m'}{a_j}\right)(\sigma+a_j)\right] sinc\left[\frac{\pi}{2}\left(\frac{m}{a_i}+\frac{m'}{a_j}\right)a_j\right]\right.$$

$$\left. + cos\left[\frac{\pi}{2}\left(\frac{m}{a_i}-\frac{m'}{a_j}\right)(\sigma+a_j)\right] sinc\left[\frac{\pi}{2}\left(\frac{m}{a_i}-\frac{m'}{a_j}\right)a_j\right]\right\} \qquad \text{(B.8.4)}$$

then

$$I_A = I_A^1 + I_A^2 + I_A^3 + I_A^4 = \frac{1}{2}\int_{-a_j}^{a_i} \mathrm{U_A} G(\sigma - \Delta_x, \lambda - \Delta_y)$$
$$* \left\{ sinc\left[\frac{\pi}{2}\left(\frac{m}{a_i} + \frac{m'}{a_j}\right) U_A\right] cos\left[\frac{\pi}{2}\left(\frac{m}{a_i}(\sigma + V_A) + \frac{m'}{a_j}(-\sigma + V_A)\right)\right]\right.$$
$$\left. + \, sinc\left[\frac{\pi}{2}\left(\frac{m}{a_i} - \frac{m'}{a_j}\right) U_A\right] cos\left[\frac{\pi}{2}\left(\frac{m}{a_i}(\sigma + V_A) + \frac{m'}{a_j}(\sigma - V_A)\right)\right]\right\} d\sigma$$
$$= \frac{1}{2}\int_{-a_j}^{a_i} G(\sigma - \Delta_x, \lambda - \Delta_y)\, L_{cos}(\sigma, V_A^1, U_A^1, a_i, a_j) d\sigma \tag{B.9.1}$$

and similarly,

$$I_B = \frac{1}{2}\int_{-a_j}^{0} G(\sigma - \Delta_x, \lambda - \Delta_y)\, L_{cos}(\sigma, V_B^1, U_B^1, a_i, a_j) d\sigma \tag{B.9.2}$$
$$I_C = \frac{1}{2}\int_{a_i - a_j}^{a_i} G(\sigma - \Delta_x, \lambda - \Delta_y)\, L_{cos}(\sigma, V_C^1, U_C^1, a_i, a_j) d\sigma \tag{B.9.3}$$

where

$V_A^1 = \sigma + a_j$	$V_B^1 = 0$	$V_C^1 = a_i + a_j$
$U_A^1 = a_j$	$U_B^1 = -\sigma$	$U_C^1 = a_j - a_i + \sigma$

Finally we have

$$I_{cos}^1(\sigma, v, a_i, a_j, \Delta_x, \Delta_y) = I_A - I_B - I_C$$
$$= \frac{1}{2}\int_{-a_j}^{a_i} G(\sigma - \Delta_x, \lambda - \Delta_y)\, L_{cos}(\sigma, V_A^1, U_A^!, m, m', a_i, a_j) d\sigma$$
$$- \frac{1}{2}\int_{-a_j}^{0} G(\sigma - \Delta_x, \lambda - \Delta_y)\, L_{cos}(\sigma, V_B^1, U_B^1, m, m', a_i, a_j) d\sigma$$
$$- \frac{1}{2}\int_{a_i - a_j}^{a_i} G(\sigma - \Delta_x, \lambda - \Delta_y)\, L_{cos}(\sigma, V_C^1, U_C^1, m, m', a_i, a_j) d\sigma \tag{B.10.1}$$

Another expression can be calculated by following all the steps,

$$I_{sin}^1(\sigma, v, a_i, a_j, \Delta_x, \Delta_y)$$
$$= \frac{1}{2}\int_{-a_j}^{a_i} G(\sigma - \Delta_x, \lambda - \Delta_y)\, L_{sin}(\sigma, V_A^1, U_A^1, m, m', a_i, a_j) d\sigma$$
$$- \frac{1}{2}\int_{-a_j}^{0} G(\sigma - \Delta_x, \lambda - \Delta_y)\, L_{sin}(\sigma, V_B^1, U_B^1, m, m', a_i, a_j) d\sigma$$
$$- \frac{1}{2}\int_{a_i - a_j}^{a_i} G(\sigma - \Delta_x, \lambda - \Delta_y)\, L_{sin}(\sigma, V_C^1, U_C^1, m, m', a_i, a_j) d\sigma \tag{B.10.2}$$

where

$$L_{sin}(\sigma, V_A, U_A, m, m', a_i, a_j) = \left\{-sinc\left[\frac{\pi}{2}\left(\frac{m}{a_i}+\frac{m'}{a_j}\right)U_A\right]cos\left[\frac{\pi}{2}\left(\frac{m}{a_i}(\sigma+V_A)+\frac{m'}{a_j}(-\sigma+V_A)\right)\right] + sinc\left[\frac{\pi}{2}\left(\frac{m}{a_i}-\frac{m'}{a_j}\right)U_A\right]cos\left[\frac{\pi}{2}\left(\frac{m}{a_i}(\sigma+V_A)+\frac{m'}{a_j}(\sigma-V_A)\right)\right]\right\}$$

with similar steps, I can obtain the expressions for I^2_{sin} and I^2_{cos} as

$$I^2_{cos}(\lambda, u, n, n', b_i, b_j) = \frac{1}{2}\int_{-b_j}^{b_i} L_{cos}(\sigma, V_A^2, U_A^2, n, n', b_i, b_j)d\sigma - \frac{1}{2}\int_{-b_j}^{0} L_{cos}(\sigma, V_B^2, U_B^2, n, n', b_i, b_j)d\sigma - \frac{1}{2}\int_{b_i-b_j}^{b_i} L_{cos}(\sigma, V_C^2, U_C^2, n, n', b_i, b_j)d\sigma \tag{B.10.3}$$

$$I^2_{sin}(\lambda, u, n, n', b_i, b_j) = \frac{1}{2}\int_{-b_j}^{b_i} L_{sin}(\sigma, V_A^2, U_A^2, n, n', b_i, b_j)d\sigma - \frac{1}{2}\int_{-b_j}^{0} L_{sin}(\sigma, V_B^2, U_B^2, n, n', b_i, b_j)d\sigma - \frac{1}{2}\int_{b_i-b_j}^{b_i} L_{sin}(\sigma, V_C^2, U_C^2, n, n', b_i, b_j)d\sigma \tag{B.10.4}$$

where

$V_A^2 = \lambda + b_j$	$V_B^2 = 0$	$V_C^2 = b_i + b_j$
$U_A^2 = b_j$	$U_B^2 = -\lambda$	$U_C^2 = b_j - b_i + \lambda$

Therefore, the result of the coupling admittance can be calculated by implementing Eqn (B.10) into (B.1) (B.2) with some fixed variables.

8 Reference

[1] O. M. Bucci and M. D. Migliore, "A Novel Nonuniform Fast Fourier Transform Algorithm and Its Application to Aperiodic Arrays," in *IEEE Antennas and Wireless Propagation Letters*, vol. 16, pp. 1472-1475, 2017.

[2] O. M. Bucci and M. D. Migliore, "A New Method for Avoiding the Truncation Error in Near-Field Antennas Measurements," in *IEEE Transactions on Antennas and Propagation*, vol. 54, no. 10, pp. 2940-2952, Oct. 2006.

[3] F. Meglio, G. Panariello and G. Schirinzi, "Three dimensional SAR image focusing from non-uniform samples," *2007 IEEE International Geoscience and Remote Sensing Symposium*, Barcelona, 2007, pp. 528-531.

[4] G. Oliveri, M. Carlin and A. Massa, "Complex-Weight Sparse Linear Array Synthesis by Bayesian Compressive Sampling," in *IEEE Transactions on Antennas and Propagation*, vol. 60, no. 5, pp. 2309-2326, May 2012.

[5] O. M. Bucci, S. Perna and D. Pinchera, "Synthesis of Isophoric Sparse Arrays Allowing Zoomable Beams and Arbitrary Coverage in Satellite Communications," in *IEEE Transactions on Antennas and Propagation*, vol. 63, no. 4, pp. 1445-1457, April 2015.

[6] I. E. Lager, C. Trampuz, M. Simeoni and L. P. Ligthart, "Interleaved Array Antennas for FMCW Radar Applications," in *IEEE Transactions on Antennas and Propagation*, vol. 57, no. 8, pp. 2486-2490, Aug. 2009.

[7] M. D. Migliore, "On the Sampling of the Electromagnetic Field Radiated by Sparse Sources," in *IEEE Transactions on Antennas and Propagation*, vol. 63, no. 2, pp. 553-564, Feb. 2015.

[8] F. C. Chen, J. F. Chen, Q. X. Chu and M. J. Lancaster, "X-Band Waveguide Filtering Antenna Array With Nonuniform Feed Structure," in *IEEE Transactions on Microwave Theory and Techniques*, Early Access, [Online]. Available: http://ieeexplore.ieee.org/stamp/stamp.jsp?arnumber=7936600

[9] M. Simeoni, I. E. Lager, C. I. Coman and A. G. Roederer, "Implementation of polarization agility in planar phased-array antennas by means of interleaved subarrays," in *Radio Science*, vol. 44, no. 05, pp. 1-12, Oct. 2009.

[10] G. Oliveri, M. Donelli and A. Massa, "Linear Array Thinning Exploiting Almost Difference Sets," in *IEEE Transactions on Antennas and Propagation*, vol. 57, no. 12, pp. 3800-3812, Dec. 2009.

[11] G. Oliveri, L. Manica and A. Massa, "ADS-Based Guidelines for Thinned Planar Arrays," in *IEEE Transactions on Antennas and Propagation*, vol. 58, no. 6, pp. 1935-1948, June 2010.

[12] R. L. Haupt, "Thinned arrays using genetic algorithms," in *IEEE Transactions on Antennas and Propagation*, vol. 42, no. 7, pp. 993-999, July 1994.

[13] D. W. Boeringer and D. H. Werner, "Particle swarm optimization versus genetic algorithms for phased array synthesis," in *IEEE Transactions on Antennas and Propagation*, vol. 52, no. 3, pp. 771-779, March 2004.

[14] R. L. Haupt, "Optimized Element Spacing for Low Sidelobe Concentric Ring Arrays," in *IEEE Transactions on Antennas and Propagation*, vol. 56, no. 1, pp. 266-268, Jan. 2008.

[15] D. H. Werner, M. D. Gregory and P. L. Werner, "Nature-inspired ultra-wideband array synthesis techniques," *2011 International Conference on Electromagnetics in Advanced Applications*, Torino, 2011, pp. 223-226.

[16] M. C. Vigano, G. Toso, G. Caille, C. Mangenot and I. E. Lager, "Spatial density tapered sunflower antenna array," *2009 3rd European Conference on Antennas and Propagation*, Berlin, 2009, pp. 778-782.

[17] M.C. Viganó, G. Toso, G. Caille, C. Mangenot, and I.E. Lager, "Sunflower array antenna with adjustable density taper," IJAP, vol. 2009, Article ID 624035, Jan. 2009.

[18] M.C. Viganó, Sunflower Array Antenna forMulti-Beam Satellite Applications, Ph.D. thesis, Delft University of Technology, 2011.

[19] A. B. Smolders, R. M. C. Mestrom, A. C. F. Reniers and M. Geurts, "A Shared Aperture Dual-Frequency Circularly Polarized Microstrip Array Antenna," in *IEEE Antennas and Wireless Propagation Letters*, vol. 12, pp. 120-123, 2013.

[20] D. M. Pozar and S. D. Targonski, "A shared-aperture dual-band dual-polarized microstrip array," in *IEEE Transactions on Antennas and Propagation*, vol. 49, no. 2, pp. 150-157, Feb 2001.

[21] S. Chakrabarti, "Development of Shared Aperture Dual Polarized Microstrip Antenna at L-Band," in *IEEE Transactions on Antennas and Propagation*, vol. 59, no. 1, pp. 294-297, Jan. 2011.

[22] M. J. Ehrlich and J. Short, "Mutual Coupling Considerations in Linear-Slot Array Design," in *Proceedings of the IRE*, vol. 42, no. 6, pp. 956-961, June 1954.

[23] V. Norwood, "Note on a method for calculating coupling coefficients of elements in antenna arays," in *IRE Transactions on Antennas and Propagation*, vol. 3, no. 4, pp. 213-214, October 1955.

[24] P. Hannan, "The element-gain paradox for a phased-array antenna," in *IEEE Transactions on Antennas and Propagation*, vol. 12, no. 4, pp. 423-433, July 1964.

[25] J. L. Allen and B. L. Diamond, "Mutual Coupling in Array Antennas," Technical Report EDS-66-443, Lincoln Lab., MIT, October 4, 1966.

[26] C. Craeye and D. González-Ovejero, "A review on array mutual coupling analysis," in Radio Science, vol. 46, no. 02, pp. 1-25, April 2011.

[27] W. Kahn and H. Kurss, "Minimum-scattering antennas," in *IEEE Transactions on Antennas and Propagation*, vol. 13, no. 5, pp. 671-675, September 1965.

[28] J. Mautz and R. Harrington, "Modal analysis of loaded N-port scatterers," in *IEEE Transactions on Antennas and Propagation*, vol. 21, no. 2, pp. 188-199, March 1973.

[29] R. Harrington and J. Mautz, "Pattern synthesis for loaded N-port scatterers," in *IEEE Transactions on Antennas and Propagation*, vol. 22, no. 2, pp. 184-190, March 1974.

[30] R. Harrington and J. Mautz, "A generalized network formulation for aperture problems," in *IEEE Transactions on Antennas and Propagation*, vol. 24, no. 6, pp. 870-873, November 1976.

[31] A. T. de Hoop, “the n-port receiving antenna and its equivalent electrical network,” Philips Research Laboratories, vol.30, pp. 302-315, 1975.

[32] T. S. Bird, "Mode coupling in a planar circular waveguide array," in Microwaves, Optics and Acoustics, IEE Journal on, vol. 3, no. 5, pp. 172-180, September 1979.

[33] T. S. Bird, "Analysis of mutual coupling in finite arrays of different-sized rectangular waveguides," in *IEEE Transactions on Antennas and Propagation*, vol. 38, no. 2, pp. 166-172, Feb 1990.

[34] M. C. Bailey, “Technique for extension of small antenna array mutual-coupling data to larger antenna arrays,” NASA Technical paper 3603, Langley Research Center, Hampton, Virginia, August 1996.

[35] C.I. Coman, “Shared aperture array antennas composed of differently sized elements arranged in sparse sub-arrays,” Ph.D. dissertation, Delft University of Technology, The Netherlands, January 2006.

[36] M. J. Mehta, “Investigation of the scanning capabilities of a shared aperture antenna array consisting of moderate bandwidth radiators”, Master thesis, Delft University of Technology, The Netherlands, July 2006.

[37] L. M. Almela, “The efficient computation of the mutual coupling in large, non-periodic array antennas,” Master thesis, Delft University of Technology, The Netherlands, June 2008.

[38] Constantine A. Balanis, *Antenna Theory: Analysis and Design. 4rd ed*. Hoboken, NJ: John Wiley, 2016.

[39] T. S. Bird, *Fundamentals of Aperture Antennas and Arrays*, Chichester, UK: John Wiley & Sons, Inc., 2016.

[40] G. A. Hockham and G. H. Walker, "Study of a Finite Phased Array Antenna," 1973 3rd European Microwave Conference, Brussels, Belgium, 1973, pp. 1-4.

[41] G. Conciauro, M. Guglielmi and R. Sorrentino. *Advanced Modal Analysis*, John Wiley and Sons Ltd., Chichester, England, 2000.

[42] D. M. Pozar, *Microwave Engineering Second Edition*, John Wiley and Sons Ltd., Chichester, England, 1998.

[43] S. J. Orfanidis, *Electromagnetic Waves and Antennas*, [Online], Available: http://www.ece.rutgers.edu/~orfanidi/ewa

[44] L. Lewine, Advanced Theory of Waveguides, London, UK: Published for Wireless Engineer by Iliffe, 1951.

[45] M. Bozzi, G. Conciauro and L. Perregrini, "On the evaluation of modal coupling coefficients by contour integrals," in IEEE Transactions on Microwave Theory and Techniques, vol. 50, no. 7, pp. 1853-1855, Jul 2002.

[46] M. J. Mehta, I. E. Lager, “Two-Dimensional Interpolation for the numerical estimation of the Mutual Couplings in large antenna arrays,” IRCTR, Delft University of Technology, 2006.

[47] M. Simeoni, E. Lager and C. I. Coman, "Interleaving sparse arrays: a new way to polarization-agile array antennas?," 2007 IEEE Antennas and Propagation Society International Symposium, Honolulu, HI, 2007, pp. 3145-3148.

[48] Z. Wang and I. E. Lager, “A complete tool for analyzing mutual couplings in nonuniform arrays of rectangular aperture radiators,” accepted in IEEE Antennas Wireless Propag. Lett.

[49] Rogers Corporation, “RO4350B™ Laminates,” [Online]. Available: http://www.rogerscorp.com/acs/products/55/RO4350B-Laminates.aspx.

[50] N. Ida, *Engineering Electromagnetics Second Edition*, New York, Springer-Verlag New York, 2004.